Nanotechnology in rubber-*myth or reality*?

Anil K. Bhowmick

Rubber Technology Centre, Indian Institute Of Technology, Kharagpur-721302, India
E-mail: anilkb@rtc.iitkgp.ernet.in

Nanotechnology is fast becoming a key technology of the 21st century. Nanotechnology can be defined as, the purposeful engineering of matter at scales of less than 100 nanometers (nm) to achieve size-dependent properties and functions. Myths are being formed on the proverbial nanotechnology market, but the reality is nanotechnology is not a market but a value chain. The chain comprises of - nanomaterials (nanoparticles), nanointermediates (coatings, compounds, smart fabrics) and finally leading to nano-enabled products (cars, clothing, airplanes, robots).

Nowadays, polymeric materials are applied in almost all areas of our life and they have a stimulating function for the development of future technologies. In contrast to metallic and ceramic materials, polymers are relatively cheap, can easily be processed, as they need less energy for production and shaping, and have a variety of fields of application in textiles, electromagnetic shielding, coatings, automotive parts, electronic and household appliances etc.

Recently, elastomer-nanocomposites reinforced with low volume fraction of nanofillers have attracted great interest due to their fascinating properties. The incorporation of nanofillers such as layered silicate clays, carbon nanotubes, nanofibers, calcium carbonate, metal oxides or silica nanoparticles into elastomers improves significantly their mechanical, thermal, dynamic mechanical, barrier properties, flame retardancy etc. The very low particle size, the high aspect ratio and large interface area yield an extraordinary improvement of the properties in a wide variety of rubbery materials. The uniform dispersion of nanofillers in elastomer matrices is a general prerequisite for achieving desired mechanical and physical characteristics. In this presentation, current developments in the field of elastomer nanocomposites reinforced with layered silicates, silica, carbon nanotubes, nanofibers and various other nanoparticles will be highlighted. New theories and models promulgated to elucidate the role of polymer-nanofiller adhesion/interaction at the interface region in extracting high-performance from such nanocomposites even at low loadings will also be addressed.

Nanotechnology commercialization is approaching a broad-ranging transformation – a phase change. The scientific advances achieved through comprehension of the different fundamental principles are reflected in the increased government funding, startup development and corporate research interest. The ramifications of the technological advancements are the decisive improvements in existing products, creation of new products and production lines with superior process alternatives and obvious disruption of competitive dynamics and cost structures. Hence, nanotechnology in rubber is no more a myth, but a

reality. However, it is necessary to establish cooperation among research institutes, funding agencies and industries as soon as possible to achieve a rapid market growth.

Polymer nanocomposites reinforced with polysaccharide nanocrystals

Alain DUFRESNE

Ecole Française de Papeterie et des Industries Graphiques, BP 65, 38402 Saint Martin d'Hères Cedex, Email: Alain.Dufresne@efpg.inpg.fr

There are numerous examples where animals or plants synthesize extracellular high-performance skeletal biocomposites consisting of a matrix reinforced by nanosize crystalline domains. Cellulose and chitin are classical examples of these reinforcing elements, which occur as whisker-like microfibrils that are biosynthesized and deposited in a continuous fashion. In many cases, this mode of biogenesis leads to crystalline microfibrils that are almost defect-free, with the consequence of axial physical properties approaching those of perfect crystals.

During the last decade we have attempted to mimic biocomposite by blending cellulose or chitin whiskers from different sources with polymer matrices. Aqueous suspensions of such nanocrystals can be prepared by acid hydrolysis of the substrate. The object of this treatment is to dissolve away regions of low lateral order so that the water-insoluble, highly crystalline residue may be converted into a stable suspensoid by subsequent vigorous mechanical shearing action. The resulting nanocrystals occur as rod-like particles or whiskers, which dimensions depend on the nature of the substrate. Starch can also be used as a source for the production of nanocrystals. The constitutive nanocrystals appear as platelet-like nanoparticles with a length ranging between 20 and 40 nm, a width ranging between 15 and 30 nm and a thickness ranging between 5 and 7 nm. Since the first announcement of using cellulose whiskers as a reinforcing phase, they were extensively used as model fillers in several kinds of polymeric matrices, including synthetic and natural ones.

Casting mixtures of polysaccharide nanocrystals and lattices led to composites with drastically enhanced mechanical properties, especially at T> Tg of the matrix, by virtue of the formation of a whiskers network, even when the whisker volume fraction was only a few percent. The formation of this rigid network, resulting from strong interactions between whiskers was assumed to be governed by a percolation mechanism. This hydrogen-bonded network induced a thermal stabilization of the composite up to 500 K, the temperature at which polysaccharides start to decompose.

In addition to some practical applications, the study of these nanocomposite materials can help to understand some physical properties as geometric and mechanical percolation effect.

Key words: nanocomposites, polysaccharide nanocrystals, cellulose whiskers, chitin whiskers, percolation

Studies on the crystalline transitions in syndiotactic polystyrene – solvent complexes

C. Ramesh
Division of Polymer Science and Engineering
National Chemical Laboratory
Pune 411008
Email: c.ramesh@ncl.res.in

Amorphous syndiotactic polystyrene (sPS) was crystallized at room temperature in norbornadiene (bicyclo[2,2,1]-hepta-2,5-diene), mesitylene (1,3,5-Trimethylbenzene), 3-carene (3,7,7-trimethyl bicyclo[4,1,0]hept-3-ene) and DMN (1,4-dimethylnaphthalene) to form the sPS-solvent complex (δ form) with respective solvent molecules. In situ HTFTIR studies showed that the δ form to γ form transformation temperature occurs well below the glass transition temperature of sPS, which is depressed due to the presence of solvent in the amorphous phase; higher the solvent content in the complex, lower the transition temperature. Glass transition temperatures determined by modulated differential scanning calorimetry (MDSC) coincide with the transition temperatures, indicating that the δ form transforms into γ form at the glass transition temperature for these complexes. Such a behavior is very different from the behaviour of the sPS- solvent complexes formed by dichloromethane, chloroform, toluene, o-dichlorobenzene, decalin (cis-trans) etc. and for these complexes the transition occur well above the Tg.

Key words: syndiotactic polystyrene, HTFTIR, modulated differential scanning calorimetry

Morphology Control and Enhancement of Mechanical Properties of Polypropylene Blends

Masayuki Yamaguchi*

Japan Advanced Institute and Technology,

1-1 Asahidai, Nomi, Ishikawa 923-1292

Email: m_yama@jaist.ac.jp

Abstract

The impact of miscibility on mechanical properties and final morphology in a set of binary blends of isotactic polypropylene (PP) and rubbery olefin copolymers are studied. It is found that the ethylene−α-olefin copolymers having more than 50 mol% of α-olefin are miscible with iPP where the copolymers are completely incorporated into the amorphous region of PP. The miscible blends show significantly high drawability with pseudo affine deformation of spherulites. On the other hands, the immiscible blends showing phase-separated morphology exhibit more brittle behavior accompanied by void formation inside the rubber domains.

Introduction

Intense studies on the structure-properties relationship for blends of isotactic polypropylene (PP) and rubbery materials have been performed in order to improve the low-temperature toughness of PP these days. According to them, ethylene-propylene copolymer and linear low-density polyethylene, which have been practically blended with PP, are immiscible with PP, although the species and contents of α-olefin unit affect the morphology of the blends (Dumoulin *et al*. [1]; Yamaguchi [2]). Furthermore, recent studies have revealed that some rubbery polyolefin materials are miscible with PP. According to our previous studies, ethylene-1-butene copolymer, ethylene-1-hexene copolymer, and ethylene-1-octene copolymer, whose α-olefin content is above 50 mol%, are found to be miscible with PP in the molten state (Yamaguchi *et al*. [3-5]). Furthermore, the copolymer chains are dissolved into the amorphous region of PP in the solid state, although the copolymers are excluded out from crystalline lattice of PP. The blends are fairly transparent, and show excellent strain recovery after removal of the stress. The purpose of this study is to clarify the mechanical properties of the miscible blends. In this work, immiscible blends, in which domains of an ethylene-α-olefin copolymer are dispersed in a matrix of PP, are also employed for the better understanding of the relationship between morphology and mechanical properties.

Experimental

Materials

A commercial grade of isotactic polypropylene homopolymer was employed in this study. The number-, weight-, and *z*-average molecular weights were M_n=4.3×10^4, M_w=2.1×10^5, and M_z=5.7×10^5. Further, two kinds of ethylene-1-hexene random copolymers, EHR33 and EHR51, produced by a metallocene catalyst system were also used. The molecular weights of EHR samples are as follows; M_n=1.5×10^5, M_w=2.5×10^5, and M_z=3.9×10^5 for EHR33 and M_n=1.4×10^5, M_w=2.3×10^5, and M_z=3.4×10^5 for EHR51, which were determined in ortho-dichlorobenzene at

135 ºC by a combination measurements of a gel permeation chromatography with an on-line viscometer. Furthermore, the contents of 1-hexene in the EHR, determined by ^{13}C nuclear magnetic resonance (^{13}C-NMR) spectroscopy, are 32.5 mol% for EHR33 and 50.5 mol% for EHR51. It is noted that both EHR samples are rubbery state at room temperature because they have no crystalline phase, and show lower glass transition temperatures.

PP and EHR were mixed in a solution of xylene at 110 ºC. The compositions in PP/EHR blends were 90/10, 80/20, and 70/30 (w/w). The polymers were precipitated from the solution into methyl alcohol and then dried in a vacuum oven. The obtained samples were compressed into a flat sheet by a compression-molding machine for 8 min at 200 ºC, and then quenched in an ice-water bath. The obtained films were annealed at 100 ºC for 5 h prior to measurements.

Measurements

Temperature dependence of tensile storage modulus *E'* and loss modulus *E"* in the solid state was measured using a dynamic mechanical analyzer at 10 Hz. The samples with dimensions of $5 \times 0.5 \times 20$ mm were quenched to -150 ºC and then heated at 2 ºC/min up to 170 ºC.

Tensile testing was carried out at a strain rate of 0.0083 s^{-1} at various temperatures.

Furthermore, rheo-optical properties were also examined in an attempt to obtain the information on the deformation mechanism. A tensile tester was set in a Fourier-transform infrared (FT-IR) spectrometer in which an infrared beam goes through a film specimen for the simultaneous measurements of stress-strain and infrared dichroism. The orientation function of *c*-axis, *i.e.*, molecular axis, of PP with respect to the stretching direction is calculated by the dichroic ratio of the 998 cm^{-1} band.

Results and Discussion

Morphology

According to our previous study (Yamaguchi *et al*. [5]), EHR33 is immiscible with PP, whereas EHR51 is miscible with PP in the molten state. Furthermore, electron microscope observation revealed that there is fairly homogeneous morphology in PP/EHR51 blend, whereas PP/EHR33 blend shows phase-separated morphology.
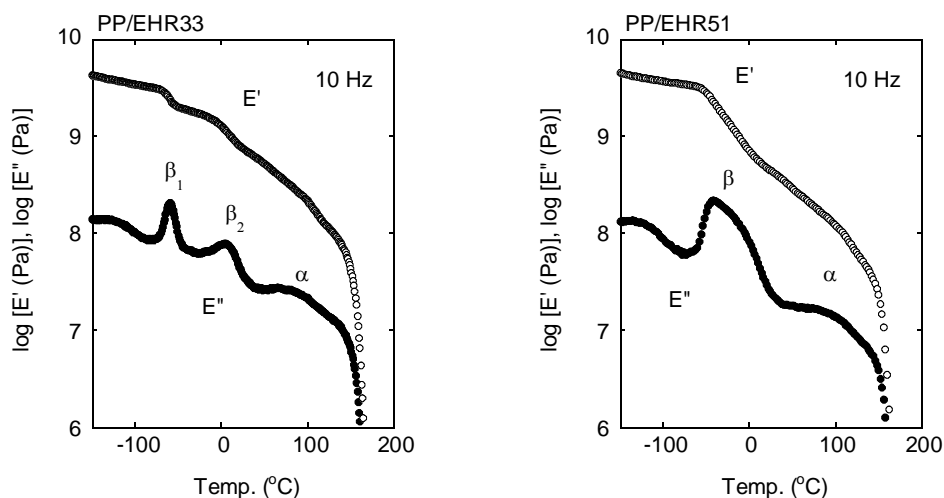

Figure 1 Temperature dependence of tensile storage modulus E' and loss modulus E" at 10 Hz for (left) PP/EHR33 (70/30) and (right) PP/EHR51 (70/30).

Figure 1 shows the temperature dependence of oscillatory tensile moduli for the PP/EHR (70/30) blends. As seen in the figure, E' decreases with increasing the temperature and falls off sharply at the glass transition temperature T_g and the melting point of PP (165 ℃). The melting point of PP is unaffected by the blending of EHR because EHR molecules are not incorporated into the crystalline lattice of PP, which is also confirmed by the measurements of wide-angle X-ray diffraction and differential scanning calorimetry. The magnitude of E' for PP/EHR33 is higher than that for PP/EHR51 in the temperature range from -40 ℃ to the melting point. The higher E' for PP/EHR33 is attributed to PP continuous phase. Furthermore, there are two relaxation peaks in the E'' curve in the temperature range between -70 and 30 ℃ for PP/EHR33: the peak located in the higher temperature is ascribed to T_g of the PP and the other peak is to T_g of the EHR. On the other hand, there is only single peak between T_gs of the individual pure components for PP/EHR51, indicating that the EHR molecules are dissolved into the amorphous region of PP.

Moreover, it was found by the small-angle X-ray diffraction measurements that the long periods, defined as the distance between the centers of two adjacent lamellae, of PP/EHR51 blends are larger than that of the PP. Figure 2 shows the compositional dependence of the long period (L_p) and the thickness of amorphous (L_a) and crystalline (L_c) layers. The L_a and L_c are calculated by the long period and volume fraction of crystallinity, assuming the two layer model. As seen in the figure, amorphous thickness increases rapidly with increasing the EHR content in the blends, which is owing to the incorporation of EHR chains into the amorphous region between PP lamellae.
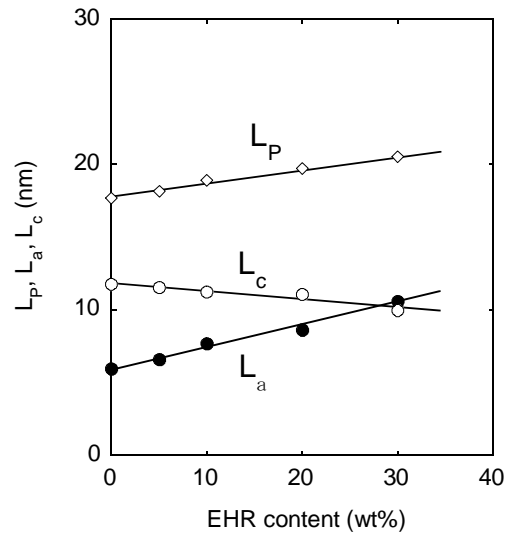

Figure 2 LP, Lc, and La for PP/EHR51 blends

Accordingly, the schematic structural model is proposed for PP/EHR51 blends as shown in Figure 3. In the figure, EHR molecules (dashed lines) are dissolved in the amorphous PP chains (solid lines).
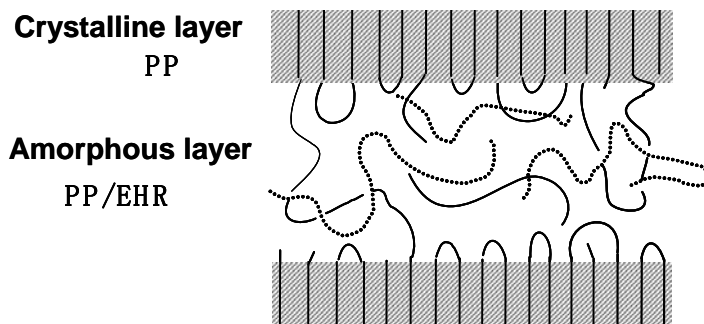
Crystalline layer
PP

Amorphous layer
PP/EHR

Figure 3 Schematic illustration of the structure for PP/EHR51. Solid lines represent PP chains and dotted lines denote EHR chains.

Tensile Properties

Table I summarizes the tensile properties of PP and the blends having 30 wt% of EHR at 25 ºC. As seen in the table, the yield and ultimate stresses of immiscible PP/EHR33 blend are higher than those of PP/EHR51 blend. The yield strain, defined as the strain at yield point, of PP/EHR51 blend is greatly larger than those of PP and PP/EHR33 blend. Moreover, it is also found that the PP/EHR51 blends show no stress-whitening in the strain region below 200 %. On the other hand, the PP/EHR33 blend shows distinct stress-whitening at the beginning of stretching, which is owing to the light scattering from the voids created by the cavitation in the EHR domains and/or segregation at the interface between PP and EHR.

Tensile properties at various temperatures were also studied. The yield and/or ultimate stresses of PP/EHR51 are found to be larger than those of PP/EHR33 at lower temperatures. Furthermore, the brittle-ductile transition of PP/EHR51 occurs at lower temperature than PP/EHR33, demonstrating that PP/EHR51 blends exhibit excellent low-temperature toughness.

Table I Tensile Properties

	Yield Stress (MPa)	Yield Strain	Ultimate Stress (MPa)
PP	38	0.19	53
PP/EHR33 (70/30)	17	0.20	30
PP/EHR51 (70/30)	13	0.58	24

Deformation Mechanism

Figure 4 shows the strain dependence of orientation function, which is estimated from the infra-red dichroic ratio of the 998 cm^{-1} band, with the stress-strain curves for PP at room temperature. As seen in the figure, the orientation function takes negative values at first and then positive values as the strain increases, indicating that molecular chains orient perpendicular at first and then in parallel in the stretching direction. The strain at which orientation function takes its minimum is near the yield point. The negative orientation below the yield point is explained by the affine or pseudo affine deformation of spherulites. The lamellar orientation to the stretching direction is responsible for the vertical orientation of the molecular chain-axis. Beyond the yield point, however, irrecoverable deformation, such as fragmentation of lamellae, rearrangement of crystalline fragments, and unfolding of folded chains, occurs. Consequently, the orientation function increases with the applied strain (Onogi *et al*. [6]).
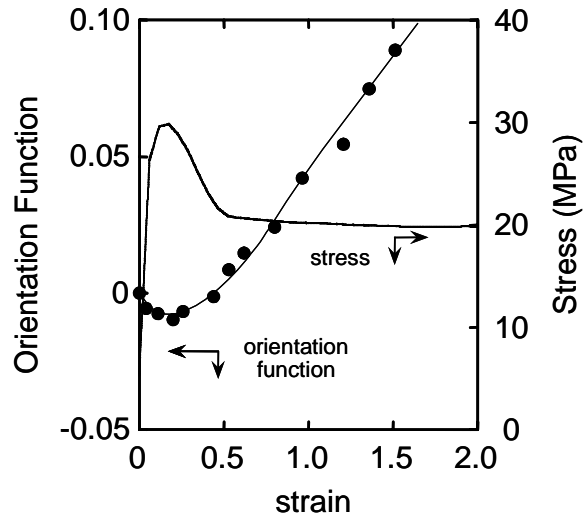

Figure 4 Growth curves of stress and orientation function for PP during stretching at room temperature

Figure 5 shows the results of the blends. There is no increase in the orientation function in the strain region for PP/EHR33 (70/30). The formation of voids, which causes the stress-whitening, leads to the complicated orientation of lamellae, instead of the affine deformation of spherulites. On the other hand, the orientation function of PP/EHR51 (70/30) shows a marked decrease and then increases after passing a minimum around a strain of 1.0. The depth and location of the blend are significantly larger than those of the PP, indicating the spherulites

deform elastically to the stretching direction to a great degree without void-opening and crazing. Such behaviors are attributed to the morphology in PP/EHR51 blends. As shown in Figure 3, rubbery EHR molecules are incorporated into the amorphous region of PP in the PP/EHR51 blends. As a result, mobility of amorphous region is enhanced, which also enhances the mobility of crystalline fragments surrounded by amorphous chains. Furthermore, tie chain fraction decreases because thickness of amorphous layer increases, as shown in Figure 2. Therefore, elastic deformation of spherulites takes place dominantly in the PP/EHR51 blends.
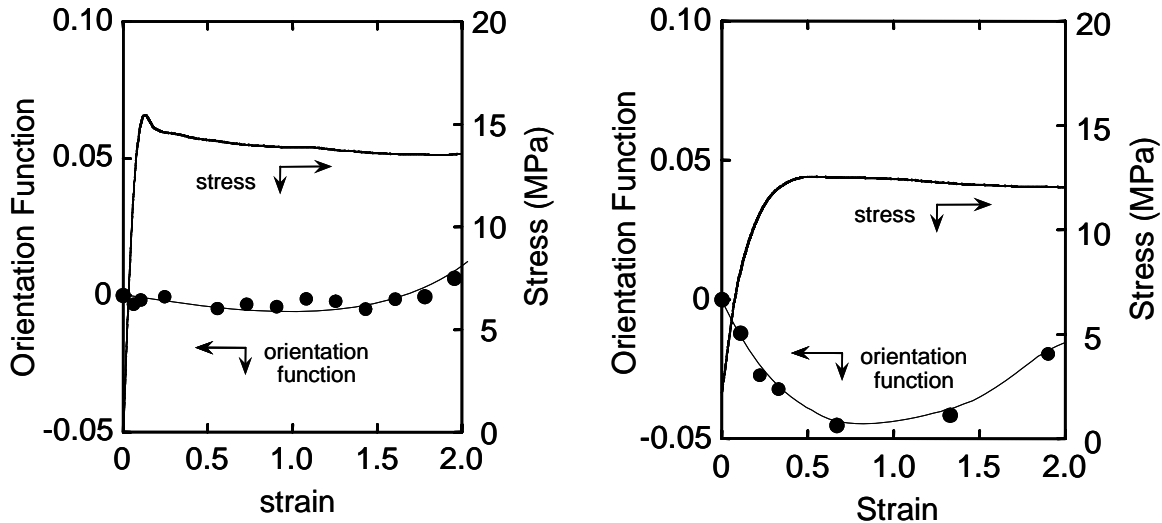

Figure 4 Growth curves of stress and orientation function during stretching at room temperature for (left) PP/EHR33 (70/30) and (right) PP/EHR51 (70/30).

Conclusion

The relationship between structure and mechanical properties for the PP/EHR blends were investigated. The following two types of blends were employed in this study: PP/EHR51 blends, in which both polymer chains are miscible in the amorphous region; and PP/EHR33 blends, in which EHR domains are dispersed in the PP matrix. It was found that PP/EHR51 blends show excellent low-temperature toughness. Furthermore, PP/EHR51 blends hardly show stress-whitening, although the distinct stress-whitening takes place in the PP/EHR33 blends. It was also found that spherulites in the PP/EHR51 blends deform elastically to the stretching direction without void-opening during elongation.

References

1. Dumoulin MM, Carreau PJ, Utracki LA. Polym Eng Sci 1987; 27:1627.
2. Yamaguchi M, J Appl Polym Sci 1998; 70: 457.
3. Yamaguchi M, Miyata H, Nitta K. J Appl Polym Sci 1996; 62: 87.
4. Yamaguchi M, Miyata H, Nitta K, Masuda T. J Appl Polym Sci 1997; 63: 467.
5. Yamaguchi M, Miyata H, Nitta K, J Polym Sci Polym Phys Ed 1997; 35: 953.
6. Onogi S, Asada T, Sakai K. Proc 5th Intern Congr Rheol Vol. 4, Ed., Onogi S. Univ. Tokyo and Univ. Park press Tokyo, 1970.

Bis-GMA/TEGDMA/clay nanocomposites: hard materials for dental restorative materials and anti scratch coatings

Behzad Pourabbas[*,#,1]**, Mehrnoosh Mahmoodian**[1]**, Shahram Mohammadpour**[1]**,**

Zohreh Ravaghi Ardebili[1] **Amirhosein Baghayee Ariya**[1] **and Paola Fabbri**[2]

1)Nanostructured Materials Research Center and Institute for Polymeric Materials, Sahand University of Technology, Tabriz 51335-1996, Iran
2)Dep. of Materials and Environmental Eng., University of Modena and Reggio Emilia, Modena 41100, Italy
Email: pourabas@sut.ac.ir

Abstract:

Photocurable acrylate based polymer/clay system of the title type has rarely been explored in the literature. The present work is a try to evaluate the said PLS system as hard materials for their applications as dental restorative materials and as anti scratch coatings for plastic sheets, PMMA. Therefore, mixture of Bis-GMA/TEGDMA (50/50 wt/wt) was used as the resin and then compounded with different clays (Cloisite93A, Cloisie30B, CloisiteNa$^+$) at different loading levels and, appropriate photo-polymerization initiators. As dental restorative materials, characterization made on blue-light cured bulk materials including investigations by TEM, FTIR and XRD, polymerization volume shrinkage, double bond conversion and standard mechanical tests including flexural strength and flexural modulus measurements. The results showed superior mechanical properties over the pure resin for Bis-GMA/TEGDMA/clay nanocomposites at 3-5 wt% loading level of Cloisite30B. The major disadvantage of the clay in such application was detected to be slightly less double bond conversion compared to the pure resin.

For coating applications, the nanocomposite precursor was applied as a thin film over PMMA slabs and then photo-cured under UV radiation. Transparent coated samples were evaluated for their scratch properties and the results were interpreted using TEM, XRD and AFM. Viscoelastic deformation was obtained for all the coatings in scratch tests with different adhesion strength to the substrate. Different interphases involved in the systems (matrix/clay, matrix/substrate and clay substrate) were detected to be the controlling factors in the final properties of the coatings. On the other hand, the interphases themselves, found to be dependent to the relative exfoliation/intercalation state in the nanocomposite, which is primarily dependent to clay type and its content. The most improved scratch properties with excellent adhesion was obtained for the samples containing 1 wt% of Cloisite30B clay.

1. Introduction

Polymer nanocomposites have been one of the highly interested subjects for innovation of new materials that can function as low-cost high-performance composites with applications ranging from automotive to food packaging and to tissue engineering [1-4]. Polymer/layered silica (PLS) nanocomposites are among this new class of materials. In which the layered clays such as modified montmorillonite (MMT) are used as the filler in production of PLS nanocomposites [5].

The in situ polymerization of monomer within the clay interspacing causes the expansion and exfoliation of the nanoclay platelets [6-8]. In the present work, it is aimed to study PLS nanocomposites of a highly cross-linkable resin mixture. The selected resin mixture is based on 2,2-bis[4-(methacryloxypropoxy)-phenyl]propane (Bis-GMA), one of the most commonly used monomers in dentistry which is able to produce hard materials upon free radical photo-polymerization after addition of suitable photo-initiators. Compared with smaller sized monomers, such as methylmethacrylate, Bis-GMA possesses the advantages

of lower volatility and diffusivity into tissues and the formation of higher moduli polymers with less volumetric shrinkage. However, Bis-GMA is a highly viscous fluid, thus the handling quality is less desirable. To overcome the lower methacrylate double bound conversation and to facilitate the mixing of fillers, a low viscous monomer, such as tri(ethylene glycol)dimethacrilate (TEGDMA) is usually added to thin the resin [9-10]. Thus, in order to evaluate the PLS nanocomposites of the said resin monomers, different PLS nanocomposites were prepared using different clays at different loadings based on a 50/50 (wt.%) mixture of Bis-GMA/TEGDMA, and their mechanical properties were examined for their application as dental composites and coating materials over PMMA substrates. Several investigation tools including TEM, XRD, FTIR, and AFM were used to characterize the dispersion state of the clay inside the matrix or double bond conversion rate and the mechanical properties including flexural modulus (FM)/ strength (FS) were measured for their applications as dental materials. The PMMA coated with different nanocomposites were investigated mainly for their scratch and adhesion properties using norma scratch tester machins.

2. Experimental
2.1 Preparation of Bis-GMA/TEGDMA based PLS nanocomposites for dental applications
To the base resin, different types of clay, polymerization photoinitiator CQ (0.2 wt %) and co-initiator 4EDMAB (0.8 wt %) were added. Before adding pohotoinitiator and co-initiator, resin and clay mixtures were mixed first by a spatula and then by magnetic stirrer and finally by ultrasonic waves for 4 min. Different formulations were prepared by using different types of clays including CloisiteNA$^{+®}$, Cloisite30B$^®$ and Cloisite93A$^®$ at different loading levels. These are encoded as resin/clay/X% where /clay/ denotes to the type of the clay used (Cs30B, Cs93A or CsNa$^+$) and /X% denotes to the wt.% of the clay in the composition.

2.2 Preparation of coating precursors and the coating process

Mixture of Bis-GMA/TEGDMA (50/50 wt.%) was prepared by mixing for 30 minutes. Then, different amounts (1, 3, 5, 7 wt.%) of different clays, were added and mixed for 2 hr. After mixing, clays were dispersed via ultrasonic waves (20 kHz, 45-50 W) at ice-water bath for 4 min. Then, UV initiator (0.5 wt%) was added and applied over the substrate with a wire wound applicator to prepare a wet thickness of 500 μm. Then they were cured using a UV wavelength emitting HPK medium-pressure mercury lamp, 125W (Philips) at 10 cm distance from the lamp during 10 min. These samples are encoded as Resin/clay/X% where /clay/ denotes to the type of the clay used (Cs30B, Cs93A or CsNa$^+$) and /X% denotes to the wt.% of the clay in the composition.

3. Results and discussion
3.1   Clay dispersion state

The original clays, CsNa$^+$, Cs30B and Cs93A have interlayer spacing as 11.7, 18.5 and 23.6 °A respectively, equal to 3.74, 4.77 and 7.54 degree respectively, on 2θ scale of a XRD diffraction pattern working at the said condition.

XRD diffraction patterns are shown for different samples in Fig. 1. As can be seen, there is not any resolvable peak on 2θ scale for coatings containing Cs30B and Cs93A at 1 and 3 wt.% loading showing a possible exfoliated state for the clay layers inside the matrix. At 5 and 10 wt.% loadings of Cs30B and Cs93A organomodified clays, an intercalation peak specially for Resin/Cs30B/10%, is appeared at lower end of the 2θ scale showing the intercalated layers inside the matrix. However, for CsNa$^+$ containing samples, with the XRD patterns provided in Figs. 1a and 1b for comparison, there is a remarkable and wide diffraction peak around 5 degree on 2θ-scale especially for 10 wt.% of clay. This suggests not only intercalation has not been occurred but also interlayer spacing has reduced with respect to the original CSNa$^+$ due to rigid matrix formation around the particles upon curing. In general, diffraction peaks in XRD diffraction patterns of PLS nanocomposites, can detect intercalated layers when the intercalated

particles are big enough however, unless otherwise, no peak can be detected as it happens in the case of exfoliated layers. Therefore, for better understanding the real exfoliation/intercalation status, TEM images should be used.

TEM images are shown in Fig. 2 for different selected nanocomposites. As can be seen, Fig. 2a confirms XRD results regarding an exfoliated state for Resin/Cs30B(1%) so that individual layers are detectable in the figure showing the exfoliated layers for this sample. However, by comparison of the TEM images in Fig. 2 it can be deduced that by increasing the clay content, the situation goes from exfoliated state to intercalated state with an increase in number of layers in intercalated zones. On the other hand Cs30B is better compatibilized with the matrix to produce better exfoliation than Cs93A. This can be related to more polar modifier cation with two polar hydroxyl groups used for compatibilization of Cs30B in comparison to that of Cs93A.

Finally, Fig. 2f confirms the XRD results for $CsNa^+$ containing nanocomposites based on contraction of the particles inside the cured matrix by means of the deformed particles shown in Fig. 2f.

3.2 Double bond conversion and volume shrinkage

Degree of double bond conversion (DC %) was determined as the ratio of IR peak areas for aliphatic C=C (1638 cm^{-1}) and aromatic C=C vibration bands (1615 cm^{-1}) before and after curing of the specimen [11]. Polymerization volume shrinkage percent at 20 $^{\circ}$C was obtained by measuring the densities before and after polymerization, according to the following equation:

$$\text{Shrinkage (\%)} = (d_{\text{after curing}} - d_{\text{before curing}})/d_{\text{after curing}} \times 100$$

where d is the density [10].

The results showed a decrease in both DC% and volume shrinkage as clay content increases in the nanocomposites. However, a different behavior was observed for samples containing $CSNa^+$ clay. This reflects the effect of clay modification and the type of modifier cation on the structural properties of the obtained nanocomposites. The clay $CSNa^+$ has no organic modifier and therefore, is less compatible with the organic matrix when compared to organomodified clays CS93A and CS30B. As a general conclusion, the decrease in DC% can be related to optical opacity of the clay layers.

3.3 Mechanical properties

Flexural strength (FS) and flexural modulus (FM) of the nanocomposites are shown in Figs. 3 and 4, respectively (all data are the average data over at least 5 measurements). Fig. 3 shows the highest FS for samples: resin/CS30B/5%, resin/CS30B/10%, resin/CS93A/5% and resin/CS93A/10%.

An interesting result is that by increasing clay content there is a jump in FS at 5 wt % of clay loading, showing the higher flexural stiffness for those samples.

The observed behavior for FS values has also been observed for comparative values of FM. Samples containing $CSNa^+$ clay, which is an unmodified clay, their mechanical properties are not comparable (are poorer) with respect to nanocomposites containing organomodified clays CS93A and CS30B. In the same manner, nanocomposites containing CS30B clay have shown relatively more desirable mechanical properties in comparison to nanocomposites containing CS93A clay.

3.4 Adhesion quality of the coatings

Fig. 5 compares optical micrograph of scratch test results for different coating systems as well as the uncoated PMMA substrate. The trace of the indenter with varying force along its 3 mm path are appeared as grooves on multiple pictures shown in Fig. 5 from which the adhesion property of the coating can be evaluated by the force resulting in detachment, destruction or delamination of the coating layer. As can be seen, the coating made up of pure resin shows no any failure suggesting a high quality adhesion to the PMMA substrate. The same result was also obtained for Resin/Cs30B(1%) so that the coating layer could resist the applied force along the groove. However, as can be seen for coatings made up of

Resin/Cs30B(3%) and Resin/Cs30B(5%) a complete detachment from the substrate is occurred at 8.7 N and 10.2 N respectively, showing a reduced adhesion quality for these samples. At higher Cs30B content, the good adhesion is retrieved so that no failure was observed for Resin/Cs30B(7%).

In contrast to Cs30B based coatings, none of the Cs93A containing nanocomposites have shown an acceptable level of adhesion as can be seen in Fig. 5b. Nanocomposite coatings containing CsNa$^+$, have shown an excellent adhesion properties as can be seen from the scratch test results in Fig. 5c. The possible reasons for the observed phenomena and the effect of clay and its content on the adhesion properties of coatings were investigated using AFM. It was obtained that clay increases the roughness of the surface and therefore, reduces the contact area and the effective interaction of the resin-substrate. The increased roughness was found to be dependent to the clay type, its content in the composition or in the other words, exfoliated/intercalated dispersion state of the clay layers.

3.5 Scratch resistant

Although, a series of information including the penetration depth, residual depth, acoustic wave emission and friction force versus normal load are obtained simultaneously by a single scratch test, we considered the residual depth to compare the scratch resistance between different coatings. The curves of residual depth versus the normal load for Resin/Cs30B and Resin/Cs93A at different wt.% of clay are shown in Fig. 6 and are compared to that of uncoated PMMA and PMMA coated with pure resin. As it is seen, these two latter samples show a very weak scratch resistance as they show a sharp increase in residual depth at lower end of the applied normal loads. However, the residual depth increases very slowly with applied load for Resin/Cs30B(1%) (Fig. 6a) indicating the superior scratch resistance of this sample not only over the uncoated PMMA but also over all other the samples. A closer look reveals a very low rate of residual depth, lower even than that of Resin/Cs30B(1%), increasing with the applied load at lower end of the load axis for Resin/Cs30B(3%) and Resin/Cs30B(5%). However, for the latter samples, there are failures that is to say, the residual depth increases catastrophically at a certain applied load (0.9 and 2 N respectively). The normal load at failure is attributed to the onset of the applied load at which the coating layer fails by any of the mechanisms including delamination, detachment or destruction (see Fig. 5).

In Fig. 6b, it can be seen that no any scratch resistance improvement can be considered for Cs93A containing nanocomposite coatings, as they show a high rate of residual depth increase even at low applied loads accompanied with an undesired adhesion properties studied earlier.

References

[1]   Giannelis EP. *Adv. Mater*. 1996; 8: 29-35.
[2]   LeBaron PC, Wang Z, Pinnavaia T.J., *Appl. Clay. Sci.* 1999**;** 15: 11.
[3]   Alexandre M, Dubois P, *Mater. Sci. Eng. Rep.,* 2000; 28: 1.
[4]   Vaia RA, Giannelis EP, *M.R.S. Bull.,* 2001; 26: 394.
[5]   Ray SS, Okamoto M, *Prog. Polym. Sci.,* 2003; 28: 1539.
[6]   Yuan-Hsiang Y, Jui-Ming Y, *Acta Materialia*, 2004; 52, 475.
[7]   Jog JP, Priya L J, *Polym. Sci. Part B Polym. Phys.*, 2002; 40(15), 1682.
[8]   Ishida H, Campbell S., *Chem Mater.,* 2000; 12 (5), 1260.
[9]   Mahmoodian M, Baghayee Arya A, Pourabbas B, *Dent. Mater.* 2008; 24**,** 514.
[10]   Reed BB, Choi K, *Polym Preprint* (1997); 38(2), 108.
[11]   Atai M, Watts DC, Atai Z, *Biomaterials*, 2005; 26, 5015.
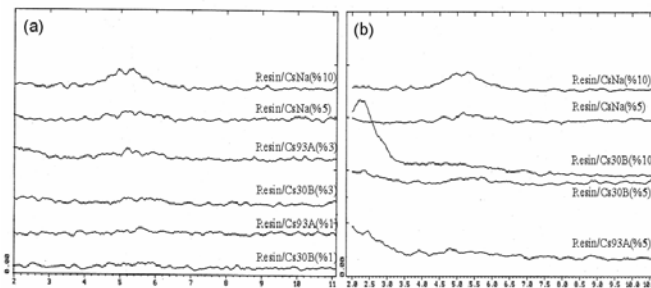[12]   Gao F, Tong Y, Schricker SR, Culbertson BM, *Polym. Adv. Tech.,* 2001; 12, 355.

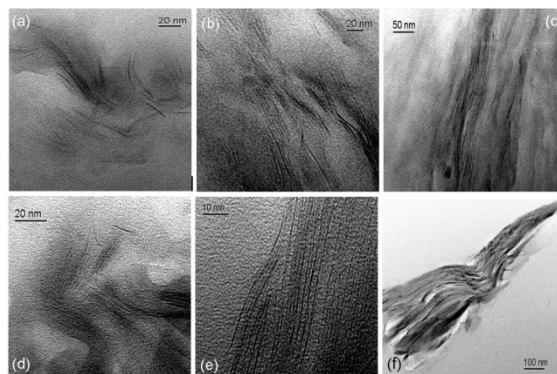**Fig. 1 Wide angle X-ray diffraction patterns for different nanocomposite coatings after curing.**

Fig. 2 TEM micrographs showing: (a) Resin/Cs30B(%1); (b) Resin/Cs30B(%3); (c) Resin/Cs30B(%5); (d) Resin/Cs93A(%1); (e) Resin/Cs93A(%5); (f) Resin/CsNa^{+}(%5).
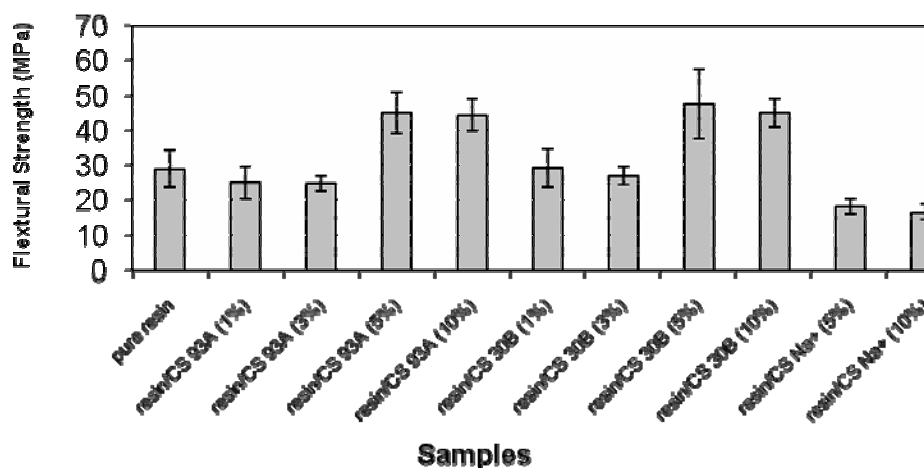

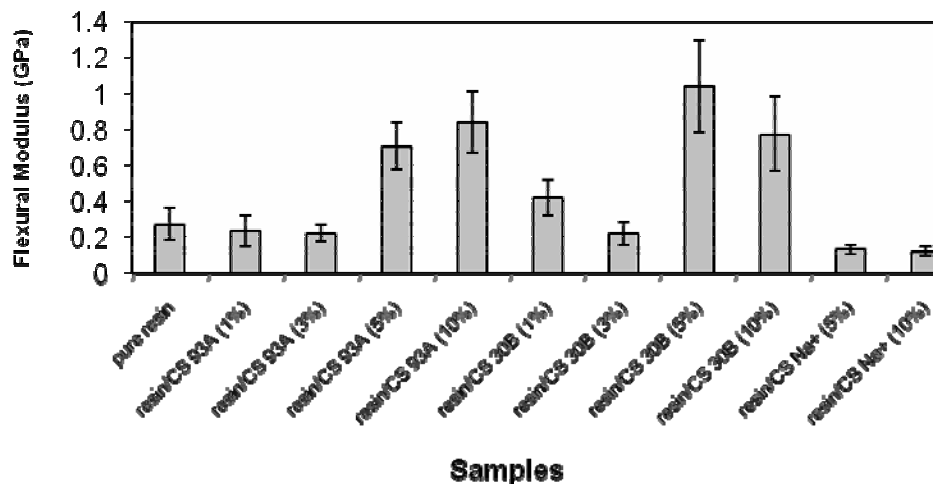**Fig. 3. Flexural strength of the PLS nanocomposites.**

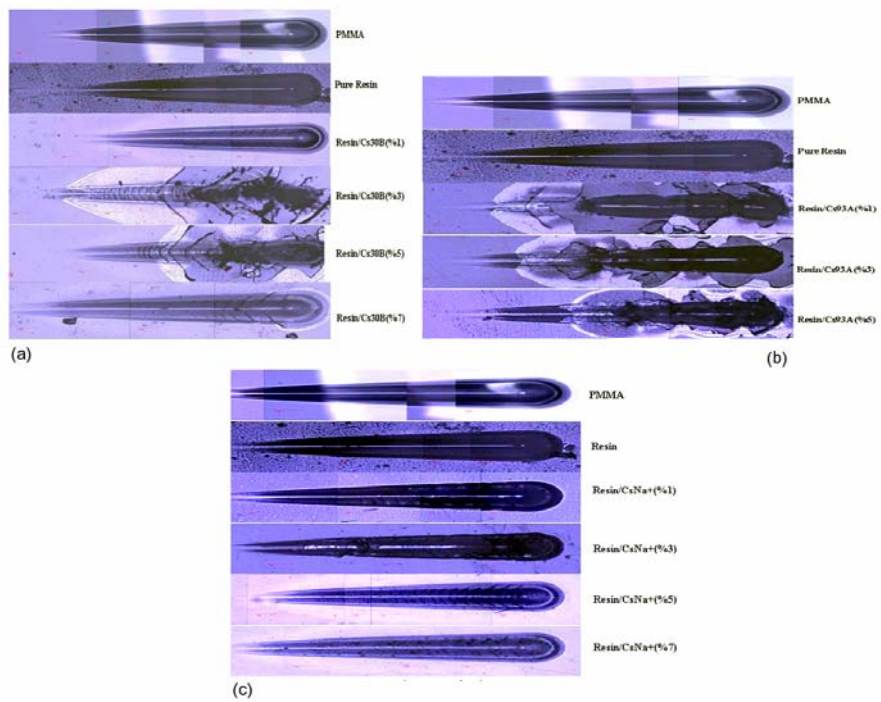Fig. 4. Flexural Modulus of the PLS nanocomposites.

Fig. 5 Optical micrograph of the scratch test results carried out on coated samples with different coating compositions as well as uncoated PMMA.
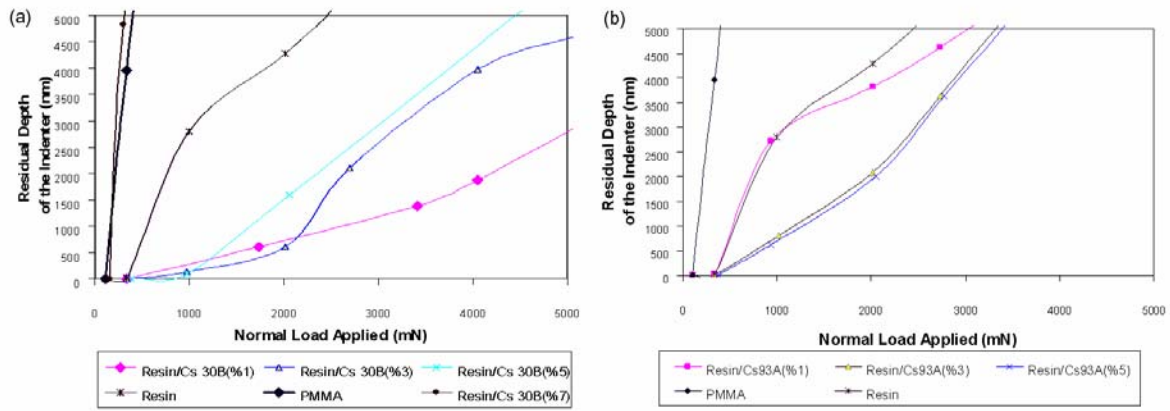
Fig. 6 Residual depth-normal load variation obtained in scratch tests for (a) Resin/Cs30B and (b) Resin/Cs93A nanocomposite coatings having different clay content. The results for uncoated PMMA and coated with pure resin are provided also for comparison.

Monte Carlo simulation of reactions in bilayer polymer blends

Darja V. Guseva,[1] Alexander V. Chertovich,[1] Arkadiy D. Litmanovich,[2] and Yaroslav V. Kudryavtsev[2],*,#

[1] Physics Department, Moscow State University, Leninskie Gory, Moscow 119991, Russia
[2] Topchiev Institute of Petrochemical Synthesis, Russian Academy of Sciences, Leninsky Prosp. 29, Moscow 119991, Russia

Email: yar@ips.ac.ru

Simulations provide a powerful tool for visualizing the processes that take place at the interphase boundaries of molten polymers. In this work, an off-lattice Monte Carlo simulation of the reaction and interdiffusion in a bilayer A/B polymer blend is carried out using the coarse-grained bead-spring model with Morse potentials. Two types of macromolecular reactions are studied: (i) polymeranalogous autocatalytic units transformation A→B (B-units accelerate the reaction) and (ii) interchain exchange.

(i) The evolution of the number density of A-units and units initially belonging to polymer A chains is studied for a compatible system. Local average characteristics of the composition distribution of reacting chains and length distribution of A and B blocks are calculated. It is demonstrated that these distributions are much broader than those for a Bernoullian copolymer of the corresponding mean composition. Such effect is due to the diffusive intermixing of reacting chains as predicted earlier for the theoretical model that describes large-scale interdiffusion in reacting polymer blends.

(ii) The evolution of the local molecular mass and block length distributions in close vicinity to a phase boundary is studied for an initially incompatible system. It is found that at the early stage the reaction takes place within a narrow interfacial layer until rather short copolymer AB blocks are formed, which then penetrate the bulk phases. In the simulation box of a finite size, a stationary state is finally formed, in which short homopolymers and copolymer blocks are distributed uniformly over the system whereas long blocks are located in the corresponding phases. At higher temperatures, this state is more homogeneous while the time of its establishment depends mainly on the interchange reaction rate.

Key words: Monte Carlo simulation, interphase boundaries, diffusive intermixing

Nonlinear elongational flow behavior of complex thermoplastic melts

Masataka Sugimoto*[#], Takashi Tanigchi, Kiyohito Koyama

Graduate School of Science and Engineering, Yamagata University

4-3-16 Yonezawa 992-8510, Japan

Tel: +81-238-26-3057, E-mail: sugimoto@yz.yamagata-u.ac.jp

Abstract

The control of strain hardening under elongational flow for polymer melts is discussed. A control of the strain hardening is strongly associated with a change of the relaxation time and relaxation time distribution. A few examples are given here. First one is polypropylene (PP). PP is a well-balanced material in terms of the physical properties such as the stiffness and heat resistance, and the cost. PP is, however, one of the linear polymers exhibit low melt strength and weak strain hardening. We focused on an introduction of a small amount of high molecular chain in order to enhance the strain hardening under elongational flow. This polymer system is very complex comparing with conventional PP. Another is poly(vinyl chloride) (PVC)/plasticizer systems. PVC forms physical gels in various solvents, and the physical properties and structure have been extensively studied mainly for low polymer concentration system. We studied the dynamic and elongational viscosity of PVC/plasticizer systems from the view point of critical gelation phenomena.

Introduction

Numerous efforts have been made on the study of the shear and elongational properties of polymer melts. The characteristics are used to describe the physical properties of a polymeric material so that we know what to expect when the polymer is processed by injection molding, film (or sheet) extruding, fiber-spinning apparatus. The two basic flows are used to characterize polymers: shear and shear-free flows. Usually polymer processings are a combination of these flows or sometimes are dominated by one or the other. The shear flow properties can be reported in many cases by manufactures and fabricators. Only this characteristic is sometimes insufficient for the processings to provide a complete picture of the relationship between the processability and the flow behavior when underwent free-surface processes in which the shape and thickness of the extrudate are determined by the rheological properties of the melt, the die dimensions etc. Therefore, we have focused attention on the melt rheology (involving elongational viscosity) control and its processability.

In this study we will report of strain hardening control of PP and PVC/plasticizer systems. Especially PP with enhanced melt strength would be typical example, since the strain hardening is not expected for conventional linear PP.

It is well known that PVC/plasticizer system forms physical gel. The structure and the physical properties have been extensively investigated. These studies are, however, mainly devoted to low polymer concentration systems. The commercial PVC compounds are generally used in rigid to flexible applications for high polymer concentration. The elongational behavior is discussed for relatively high PVC concentration systems in terms of the critical gelation temperature. The elongational behavior of sol-gel systems has not so far been reported to the best of author's knowledge.

Experimental

All the commercial samples (conventional PP and NEWSTREN/NEWFOAMER of high-melt-strength PP grades) were supplied by Chisso Petrochemical Co. (Chiba, Japan). Four grades of PPs were used: PP-A, PP-B, PP-C, and PP-D. One was conventional homogeneous polymer HT1050 (PP-A), and the others (high-melt-strength PP containing a small amount of ultra-high molecular weight component) were synthesized by series polymerization method using a Ziegler–Natta catalyst.

Two PVC/DINP samples (coded as PVC8) with different PVC concentrations were supplied from Advance Plastics Compounds Co. (APCO), Japan. Weight-average degree of polymerization of PVC used was 1,300. This PVC sample was synthesized by suspension polymerization. The PVC powder was blended with prescribed amounts of DINP, a small amount of Ca-Zn type stabilizer, and 5 pph of CaCO3, calendered on a hot roller for 5 min at 150 °C, compression molded at 180 °C under a pressure of 15 MPa, and cooled gradually to room temperature. The weight ratio of PVC/DINP in PVC8 was 0.455/0.545. These PVC compounds have a similar composition with industrial PVC/plasticizer systems.

Linear viscoelastic measurements were carried out at various temperatures between 150 °C and 220 °C with a strain-controlled rheometer (ARES, TA Instruments). Parallel-plate fixtures were utilized. The plate diameter (25 or 50 mm) was chosen according to the magnitude of the sample moduli. Elongational viscosity measurements were performed with ARES using elongational viscosity mode at several temperatures between 160 °C and 220 °C. Strain rates were from 0.05 to 1.0 s^{-1}. Here, we carried out rheological measurements for the freshly prepared PVC8 samples that was charged in the rheometer and heated to experimental temperature without experiencing higher temperatures.

Results and Discussion

Fig. 1 shows G' and tan δ plotted against angular frequencies for PP-A, B and C. G' of PP-B and PP-C was significantly higher at low frequencies in comparison with that of PP-A and slightly lower than that of PP-A at relatively high frequencies. The height of the shoulder increased with the increasing content of uhmw component. Figure 1 also exhibits an increase in the elastic response at low frequencies of high-melt-strength PP (PP-B and C), that is, a decrease in tan δ. decreasing frequencies, tan δ curves of PP-B and C culminated in the vicinity of 10^{-2} rads^{-1}, whereas that of PP-A kept rising.

Fig. 2 shows the nonlinear relaxation modulus $G(t,\gamma)$ of PP-A for γ= 0.3~ 6. The solid line represents the relaxation modulus in the linear regime, $G(t)$, which can be written by a sum of exponential function. In Figure 1, we note agreements between $G(t)$ and $G(t,\gamma)$ for a strain of 0.3 over the entire measurement time. We indicate the stress relaxation behavior of PP-C as a example of PP containing small amounts of high molecular mass chains. The nonlinear relaxation moduli for PP-C are shown in Figure 3. $G(t,\gamma)$ for γ = 0.3 agreed with the linear function $G(t)$ evaluated with dynamic viscoelasticity. Within a short time (<10^2 s), $G(t,\gamma)$ in all of the strains imposed here decreased monotonically as a function of time, and the shape was almost the same as that of PP-A. Note that the feature of $G(t,\gamma)$ for PP-C was distinctly different from that of PP-A over a certain time. Within a longer time region (>10^2 s), two-step relaxation processes attributed exclusively to the long relaxation mode were observed for the whole strain range examined. A similar behavior was obtained also for PP-B, although it is not shown here. We refer to the first relaxation step as the fast process and the second step as the slow process.

Figures 4 and 5 illustrate $\eta_E^+(t, \varepsilon')$ for various rates at 180 °C for PP-A, and -C, respectively. The solid lines in the figure are the 3-fold linear viscosities $3\eta^+(t)$. The elongational viscosities of PP-A increased smoothly for various elongational strain rates. There was no upward deviation from the linear viscosity within the strain rates measured; η_E^+ was independent of the strain rates. η_E^+ of PP-A had a tendency to follow the linear viscoelasticity rule: $\eta_E^+ = 3\eta^+(t)$ in the limit of steady state ($t\text{->}\infty$). Likewise, η_E^+ for PP-C increased smoothly with time within small strains. The sample which contains a small amount of high molecular weight components, however, exhibited remarkable upward deviations in η_E^+ called "strain hardening", depending on the elongational strains. This is unexpected behavior for conventional linear PP as mentioned before.

Figures 6 and 7 respectively show the ω dependence of G' and tan δ for the PVC8 at different 6 temperatures: 150, 160, 170, 180, 190, and 200 °C. Each measurement was performed for the freshly prepared PVC8 in order to avoid the influence of thermal history and the thermal degradation. At low temperature, $T = 150-180$ °C, PVC8 behaves as a well-developed gel; G' and G'' tend to level off with decreasing ω and exhibit a plateau at low ω. This behavior suggests that a network structure of PVC molecules is formed in PVC8. At the highest temperature of 200 °C, this system behaves as a sol, although the terminal flow behavior ($G' \propto \omega^2$ and $G'' \propto \omega$) can not be observed. At the intermediate temperature of 190 °C, the slopes of log G' and log G'' versus log ω curves become linear, indicating behavior of critical gels. These curves apparently correspond to the curves at the gel point. Figure 7 shows the plots of tan δ versus ω at various temperatures. Specifically, it suggests that the ω-independent tan δ is observed at 190 °C. This "flat" phase angle region covers a wide frequency window, as marked by a horizontal line. Only the low frequency "flat" region is associated with the gel point.

Figures 8 and 9 show the time evolution of the elongational viscosity η_E^+ of the PVC8 at various strain rates at 160 °C and 190 °C, respectively. On start-up of elongational flow at a rate, the viscosity growth function η_E^+ of PVC8 followed the linear $3\eta^+(t)$ at a short time scale, and then deviated from $3\eta^+(t)$. At 160 °C of the PVC8, the curve obtained at strain rate of 0.05 s^{-1} agrees with $3\eta^+(t)$ below 10 s. At longer time, the η_E^+ curve increases with time. The η_E^+ curves at higher strain rates increase steeply with time. None of the curves approaches steady-state values. At the critical gel temperatures (190 °C), it should be noted that all η_E^+ curves at various rates did not show large deviation from $3\eta^+(t)$ any more, though the data were scattered because of low viscosity. We can say that there is a critical change in the elongational flow behavior in the vicinity of the temperature, where the loss tangent shows independency of the frequency under shear flow. It is experimentally demonstrated that the rheological behavior of PVC/DINP systems not only shear but also elongational flows changes drastically before, near, and beyond the sol-gel transition as a function of temperature.

Concluding remarks

The nonlinear elongational flow behaviors of complex thermoplastic melts were discussed. We demonstrated that the strain hardening is caused by a presence of long relaxation time components such as very high molecular weight chain and physical crosslinks connected polymeric chains into three-dimensional network.
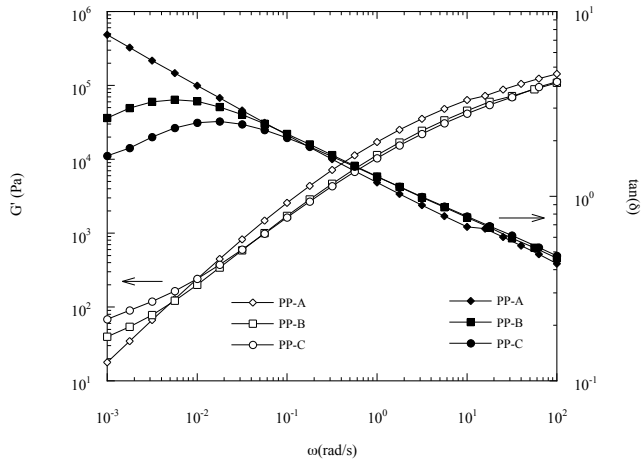
Fig. 1 G' (left y axis, closed symbols) and tan δ (right y axis, open symbols) curves plotted against the frequency measured at 180 °C for PP-A PP-B, and PP-C.
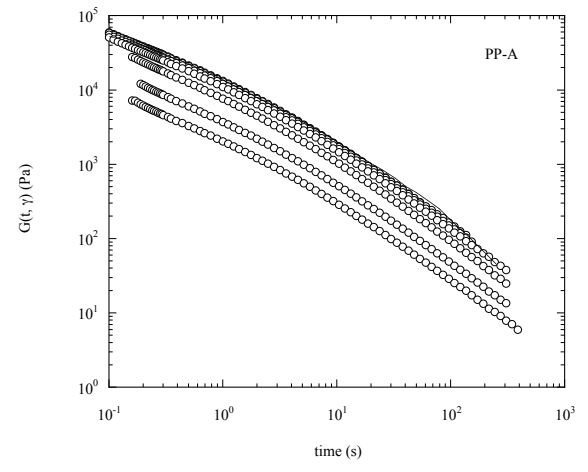

Fig. 2 $G(t,\gamma)$ of PP-A at 180 °C for various strains, 0.3, 0.5, 0.7, 1, 2, 4, and 6, from top to bottom. The solid curve represents $G(t)$ determined from the dynamic viscoelastic data.
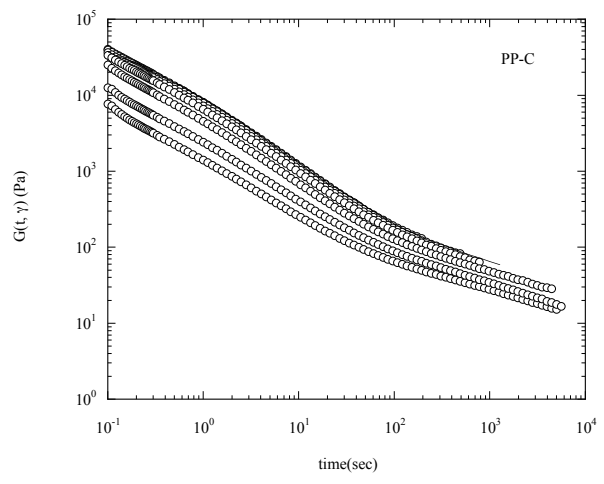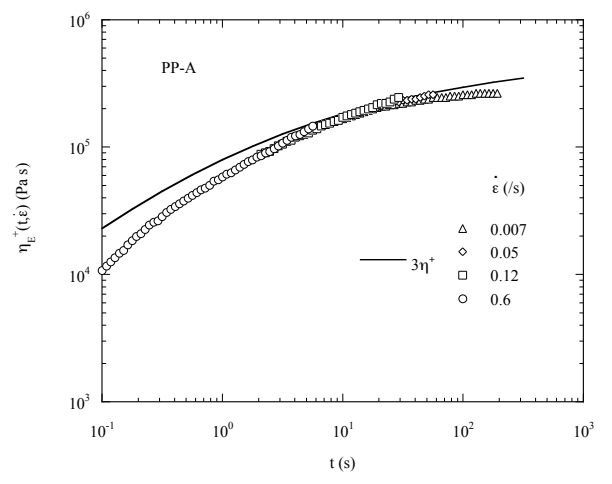

Fig. 3 $G(t,\gamma)$ of PP-C at 180 °C for various strains, 0.3, 0.5, 0.7, 1, 2, 4, and 6, from top to bottom. The solid curve represents $G(t)$ determined from the dynamic viscoelastic data.

Fig. 4 Variation of transient uniaxial extensional viscosity with time at constant strain rates and temperature of 180 °C for PP-A. The solid line indicates 3 times the dynamic viscosity, $3\eta^+$, at 180 °C.
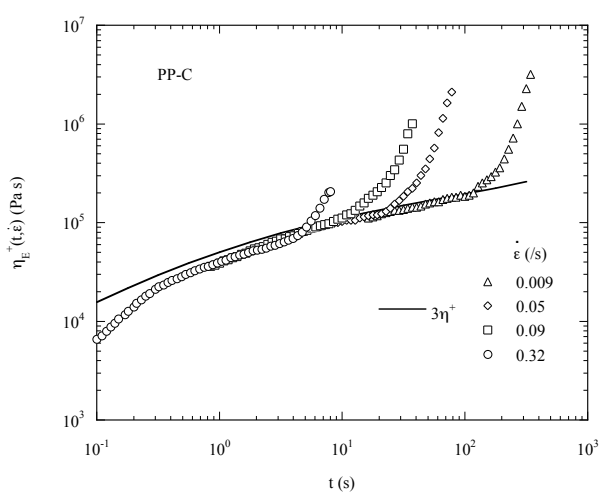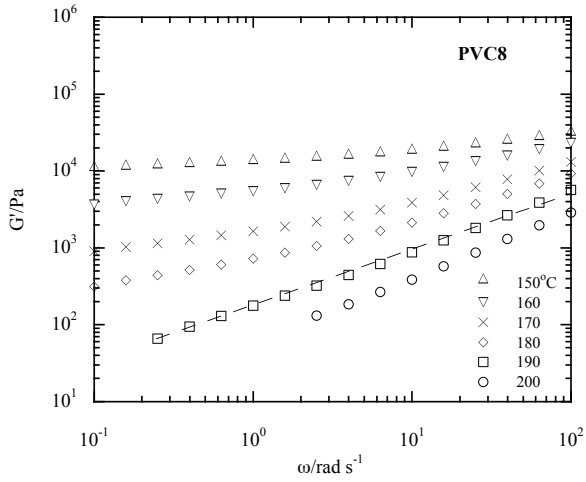

Fig. 5 Variation of transient uniaxial extensional viscosity with time at constant strain rates and temperature of 180 °C for PP-C. The solid line indicates 3 times the dynamic viscosity, $3\eta^+$, at 180 °C.

Fig. 6 Storage modulus G' of PVC8 plotted against angular frequency ω for various temperatures.
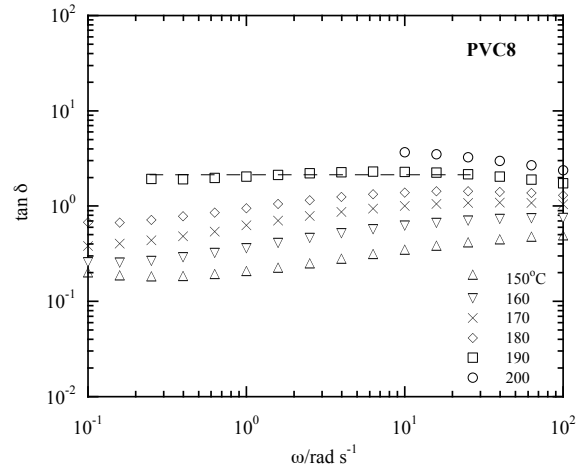

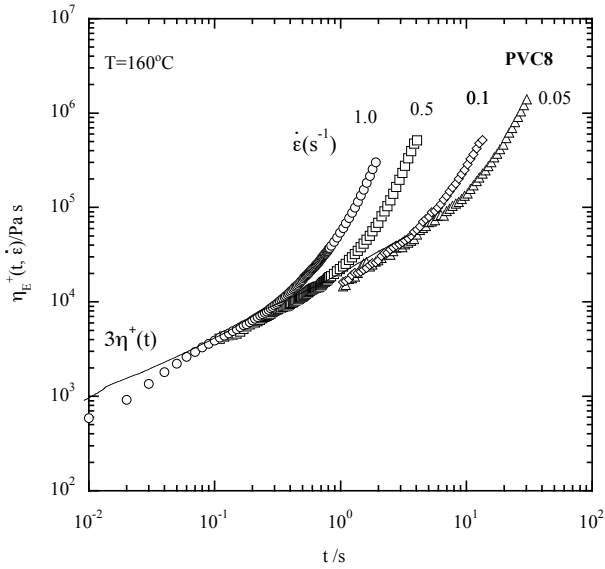Fig. 7 Loss tangent tan δ of PVC8 plotted against angular frequency ω for various temperatures.

Fig. 8 Time dependence of uniaxial elongational viscosity at various strain rates for PVC8 at 160 °C. The solid line is $3\eta^+(t)$ calculated from dynamic viscoelastic data in shear.
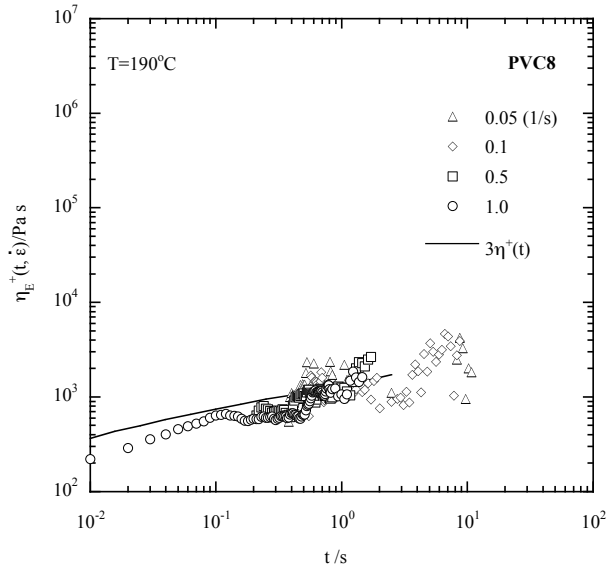

Fig. 9 Time dependence of uniaxial elongational viscosity at various strain rates for PVC8 at 190 °C. The solid line is $3\eta^+(t)$ calculated from dynamic viscoelastic data in shear.

Preparation polyamide-12 composites powders for SLS and its sintering characteristics

Jingsong Yang; Yusheng Shi; Chunze Yan

State Key Laboratory of Materials Processing and Die & Mould Technology, Huazhong University of Science and Technology. Wuhan 430074,Hubei, China.

Abstract:

Polyamide-based composites have been proven to have great potential for the RP industry to fabricate functional parts; however, it is difficult to disperse the reinforcements such as whiskers and nano-fillers to the powder uniformly by mechanically mixing, more importantly, the SLS process limits the particle diameter to smaller than 100 μm and near sphericity. This paper reports a new method for preparing polyamide-12 composite powders for applications in selective laser sintering (SLS) by using a dissolution-precipitation process. The potassium titanium whiskers (PTW), nano silica, montmorillonite and glass bead polyamide composites powders were obtained. The characteristics of the composites powders would be evaluated. The sintering characteristics and mechanical properties were also compared to pure polyamide-12 and glass filled polyamide-12.

Keywords：

Selective laser sintering (SLS), Polyamide-12, Composites dissolution-precipitation, powder

1. Introduction

Rapid prototyping (RP) techniques have been developed very quickly since its first appearance. Traditionally, these techniques have been focused on the area where the primary interest was in generating a physical model of a component or system for visualization purposes. More recently, RP has evolved to be applied to the manufacture of functional components, which require a prototype to have sufficient mechanical integrity and surface quality for handling and demonstration purposes[1-3]. Mechanical properties become critically important, and they must be comparable to those produced by using traditional manufacturing routes to make the RP-based processes competitive.

Selective laser sintering (SLS) technique is one of the processes most widely used in RP.

The SLS process is described in Figure 1[4,5]. This process is based on the layer-by-layer principle. After a SLS system distributes polymer powder in a layer over the "part bed," the sintering process uses the laser to melt the powder and the fluid flows together to create the object. In the unsintered areas, the powder remains loose and serves as a natural support for the next layer and the whole object under fabrication; hence, no additional support structure is required. Often, before the powder is sintered, the entire powder bed is heated in order to minimize thermal distortion and facilitate adhesion to the previous layer. As the process is repeated, layers of powder are deposited and sintered until the object is complete.

Polyamide-based composites have been proved to have great potential for the RP industry to fabricate functional parts[5-8]; however, the strength of classic sintered polyamide12 is only about 80% that of the injection molded polyamide specimen. This SLS process limits the particle diameter to approximately 100 μm or smaller. The polymer particles in the commercial glass bead filled polyamide have an average diameter of 48 μm; this makes fiber reinforcement difficult.

For these reasons, significant research effort has been directed towards finding SLS materials with improved mechanical properties[5,9-12]. Whiskers and nanoparticles were proved to be effective reinforced materials and widely used in polymer composites now.

Potassium titanate whiskers (PTW, $K_2O•6TiO_2$) is a class of reinforcing materials owing to their excellent chemical stability and mechanical properties[13, 14]. In particular, its mechanical properties are much superior to the traditional reinforcing materials such as glass fiber[15,16] or carbon fiber, in addition to their small dimension and a favorable length to diameter ratio with an average diameter of 1–2 μm and length of 10–40 μm. Furthermore, it does not remarkably increase the melt viscosity, showing great potential to act as reinforcing filler, and it has been successfully applied to polypropylene, polyamide, polyvinyl chloride, polycarbonate, polytetrafluoroethylene, and rubber.

Nanoparticle reinforced polymers improved properties while remaining processible, nanoparticles increase tensile modulus and strength, however, they boost these properties without reducing impact resistance. In addition, they raise the heat distortion temperature and allow current thermoplastics to find new applications. These and other improvements occur with small volume fractions of the nanoparticles, therefore, nanocomposites are lighter than

conventional composites. Using nano material in SLS processing could help change rapid prototyping into rapid manufacturing.

However, as the small dimension and special structure of whiskers and nanaparticles, it is very difficult to distribute them uniformly into polyamide powders by mechanical mixing[17]. Furthermore, their structure would have a negative effect on the sintering characteristics. Therefore, this paper studies on the methods of preparing potassium titanate whisker (PTW) reinforced PA12 composites powder(PA/PTW), PA12/clay composites powder (PA/clay), PA12-elastermor alloy/nanosilica composites powder (PAE/NSi) and glass bead filled PA12 powder (PA/GF) for application to SLS and research their effect on sintering characteristics.

2. PA12/GF composites

The shape of glass bead is spherical and can be distribute well to PA 12 powder, then PA12/GF composites can be obtained by blending glass with PA12 powder. The laser sintering characteristics of the composites is very good.

The mechanical properties of the PA12 and PA/GF samples are listed in Table 1. For the PA/GF (40 wt %), the tensile strength remained constant, while the bending strength increased by 19.5%, and the bending modulus increased by 61.4% with respect to PA12. However, this result is unsatisfactory because the impact strength significantly decreased. The impact strengths of the PA/GF(40 wt%) are only 50.3% that of PA12.

Figure 2 shows the SEM images of PA 12 and PA/GF sample impact fracture. The surface is coarse for PA12 samples and smooth for PA/GF samples except that there are many pull-out glass beads and holes. This indicates that the glass bead is not firmly fixed with polyamide-12. Consequently, the mechanical properties of the PA/GF samples are unsatisfactory.

2. PA/PTW composites

2.1 Preparation of powders

As it is very difficult to distribute PTW uniformly into PA12 powders by mechanical mixing[20] and the PTW structure would have a negative effect on the sintering characteristics[16], other methods should be developed to prepare PA/PTW composite powder. Therefore, this paper reports a new method for producing PA/PTW composite powder in

which PTW is coated by polyamide 12 in a dissolution-precipitation process[18,19].

The procedure of the dissolution-precipitation is as follows: add polyamide 12, PTW, solvent, and additives into a 10 L high-pressure reactor; pump out the oxygen; stir when the temperature reaches 150°C for 1–2 h; then, cool at the rate of 10°C/h to 105°C until polyamdide 12 begins to precipitate; maintain the temperature at 105°C until the precipitation is complete within 20 min; stop stirring and distil solvent.

2.2 Characteristics of powders

A proper particle diameter and distribution are necessary for selective laser sintering. From previous studies[9], a particle diameter of 30–50 μm was found to be ideal. If it is smaller than 20 μm, spreading the powder becomes difficult; if it is larger than 60 μm, the smoothness and precision of the SLS parts and the sintering characteristics deteriorate. Figure 3 shows the images and distribution of the PA12 and PA/PTW powders produced by dissolution-precipitation. The powder characteristics are shown in Table 2.

From Figure 3(a), the average diameter of the PA12 powders is 34.9 μm, and the distribution is wide. 7.3% of the particles are smaller than 20 μm and 8.6% are larger than 50 μm. On enlarging the particle image, it is found that the particle surface is not smooth.

The PA/PTW (10 wt.%) powders exhibit a narrow particle diameter distribution, as shown in Figure 3(b), with an average particle diameter of 36.7 μm. It can be explained that PTW act as heterogeneous nuclei[20,21] and change the precipitation process of polyamide during the cooling period, which would tend to produce powders of uniform diameter. Most parts of the surface are smoother than those of PA12 powders while others are rough; in particular, there are some very small pores in the PA/PTW (10 wt%) particles. This may be because the precipitation is too fast so that some solvent is trapped in the PA/PTW particles.

The PA/PTW (30 wt%) powders are shown in Figure 3(d). The particle diameter distribution is not uniform; it exhibits two peaks: The main peak is at 40.69 μm and the other is at 19.80 μm. The surfaces of the particles are very rough and there are many pores in the particles. This appears to be the result of the random conglomeration of many small particles.

This can be explained as follows: PTW tends to aggregate, and it is difficult to be dispersed well in the solvent as its concentration increases[17]. The PTW spreads directionally and there are several growing points for one particle. Polyamide12 precipitates around these

growing points; as a result, a large particle resembles a random conglomeration of several small particles. When the solvent trapped by polyamide12 is eliminated, the pores appear. The small peak at 19.80 μm in the particle diameter distribution for PA/PTW (30 wt%) would be the contribution of the dispersed PTW (that have not aggregated) or the PTW that possess a smaller number of growing points.

There is no free PTW in the powders shown in Figure3 (b–d); this indicates that all the PTW are coated by polyamide12 in PA/PTW powders. This result is also confirmed by the EDX analysis shown in Figure4.

The apparent densities of the PA12 powders and the PA/PTW powders are listed in Table 2. The highest density is observed for the PA/PTW (10 wt%). It is consistent with the shape of the particles. The smoother the particles are, the higher the apparent density is. The number of pores in the particles increases with the PTW percentage; this is the reason why the apparent density declines as the percentage of PTW increases.

2.3 Laser sintering characteristics

Before the powder is sintered, the entire powder bed is heated in order to prevent the sintering part from distorting by minimizing the temperature difference between the sintered parts and the surrounding environment. A higher temperature of the entire powder bed, which is known as the part-bed temperature, would decrease the crystallization speed; hence, the shrinkage stress can be released freely and distortion is prevented.

There is a range of part-bed temperatures called the sintering temperature window at which the powder can be sintered without distortion and the polymer powder will not coalesce spontaneously.

Moreover, the minimum sintering temperature is restricted by many other factors such as the powder shape, particle diameter, crystallization speed, and thermal transition of the polymer. Therefore, the available sintering temperature is much narrower than that calculated theoretically. It can be obtained by measuring the lowest agglomeration temperature and the highest distortion temperature of the powder. The previous reports[9,22] and this researches both show that the available sintering temperature window (ΔT_1) is only 1–2°C. The available sintering temperature of N12 is 168–169°C. Among all the fillers, glass bead can extend the sintering temperature window. Its available sintering temperature is 167–170°C. This is one

of the most important reasons that PA/GF is the only polyamide12 composite that is now commercially applied. The available sintering temperature window is listed in Table3

For all fillers, globular fillers such as glass bead are favorable for sintering, but fibrous fillers such as PTW are not favorable. Because of its large length to diameter ratio, PTW significantly affects the sintering characteristics. The PA/PTW powders with 10–20 wt% PTW have as good sintering characteristics as PA12 powders. The sintering layer has a regular boundary and smooth surface without distortion. When the content of PTW reaches 30 wt%, the sintering layer surface is smooth but the boundary is zigzag. This would not affect the SLS process but the side of the sample is not sufficiently smooth (Figure 5). However, for PTW filled polyamide 12 powders with 20 wt% PTW, the sintered region distorts due to the presence of many pores. It affects the sintering process so seriously that the process cannot be continued.

From above, conclusion can be made that the shape of the particles greatly affects the sintering characteristics. If the fillers are coated well by polyamide12 such as PA/PTW powders, the sintering characteristics are only determined by the composite powder particles whose shape is determined by the PTW content: if the PTW content is small (less than 10%), the shape of the particles is regular and good sintering characteristics are obtained. However, with an increase in the PTW content, the particle shape becomes irregular and the sintering characteristics deteriorate.

2.4 Mechanical properties

The mechanical properties of the PA/PTW samples are listed in Table 3. The mechanical properties improved significantly. For the NPC (20 wt%) samples, the maximum tensile strength, bending strength, and bending modulus increased by 55%, 118% and 158% with respect to N12, respectively. The impact strength is 89.3% that of the N12 samples but 169% that of the GFN (40 wt%) samples.

From above, we can conclude that PTW is much better than the glass used as a reinforcing filler for polyamide12 in the SLS process. However, the amount of PTW used is small. The maximum amount used is only 20%, but for glass it is 40%–50%. If PTW is used in injection molding, the maximum amount used is 30%–35%[20]. This can be explained by the following morphology analysis of the impact fracture surface.

The impact fracture of NPC samples are shown in Figure 6. The surface is not regular as there are some cracks and pores. Although there are pull-out whiskers, as shown in Figure 6(b), the whiskers surface is coarse and most of the whiskers are coated by polyamide12. This indicates that PTW exhibits better bonding to polyamide12.

As listed in Table 3, the optimum amount of PTW is only 20%. This can be explained from Figure (c, d) as follows: the pull-out whiskers aggregate; however, as is well known, the fillers must be dispersed well in order to acquire the optimal properties.

It is observed that pores exist in the region in which the PTW aggregate, indicating that PTW aggregate induce defects in the SLS parts. Because of these pores, the density of PA/PTW powders decreases and their mechanical properties deteriorate.

3. PA12/clay composites

There are two methods to prepare PA12/clay composites: blending and dissolution-precipitation. Figure 7 is the SEM images of powder of PA12/clay (3 wt%) composite obtained from dissolution-precipitation.

Although the shape of the particles is near globular, the density of the powder is only 0.26 g/cm^3, as the particle is porous. It may be that clay can absorb much solvent, polyamide 12 precipitation around this clay which absorbed much solvent, when the solvent is eliminated, the pores appear.

At low density, the sintering characteristics of PA/clay are deteriorated. When sintered by laser, the melt viscosity is much higher than PA 12 and it distorted even the part-bed temperature reach to 170°C. It maybe that shrinkage increased by porosity.

Then clay is blended with PA12 powder, and sintered by laser to fabricate specimens. The sintering temperature is 169~170°C, the mechanical properties of the mixed PA12/clay (3 wt %) SLS specimens are listed in Table 4. From Table 4, the tensile strength, flexural strength and impact strength of the PA/clay (3 wt %) SLS specimens are all higher than those of the PA12 SLS specimens. From the above results, it can be concluded that clay has a reinforcement effect on PA12 SLS parts.

4. PA 12-elastermor alloy/nano-silica composites

As the high sintering temperature of PA12, thermal oxidation ageing is remarkable and most of the recycled powder have to be rejected. Then PA12-elastermor alloy which can be

sintered at lower temperature and was developed for SLS. The mechanical properties of the PA12-elastermor alloy samples are listed in Table 5.

From table, the density, tensile strength, flexural strength and flexural modulus of the PAE alloy SLS specimens are all lower than those of the PA12 SLS specimens. But the impact strength increased.

In order to increase the strength, nano-silica was used. First, nano-silica was added to the solvent in the process of preparation of PAE alloy powder. But the nano-silica absorbed so much solvent that the powder is porous. Then nano-silica was blended with PAE and milled in a ball grinder. After milling, the fluidness of the powder become good as nano-silica is a good dispersant.

The sintering characteristics and mechanical properties of PAE/NSi are listed in table 5. Contrast to PAE, the tensile strength, flexural strength and flexural modulus of the PAE alloy SLS specimens are all increase notably.

Figure 8 shows the SEM images of PAE and PAE/NSi(0.5%), from figure 8, the PAE shows ductile fracture, and PAE/NSi shows brittle fracture. It indicates that nano-silica change the composites structure, it can be testified by X-ray diffraction (XRD).

Figure 9 shows the XRD of PA12 powder. In the figure, there is one main peak at 21.6 [º2Th] for PA12, the secondary peak at 37.4[º2Th]. Figure 10 shows the XRD of PAE alloy powder. Tthe main peak splits, the height are only one half PA12, and there are three secondary peak at round 40[º2Th]. But for PAE/NSi composites powder (shows in figure 11), there is only one main peak, and the new secondary peak reduced. It indicate that nano-silica promote the crystal of PAE alloy. The increasing of sintering temperature can be the result of promote crystal and increase viscosity. From table we can conclude that nano-silica has a good reinforcement effect on PA12 SLS parts.

5 Conclusions

As the strength of classic sintered PA12 is low, PA 12 based composites are researched in this paper. The method of preparing PA/GF, PA/PTW, PA/clay and PAE/NSi for application to SLS were developed, and their SLS components are made for the various applications. The PA/GF has good sintering characteristics. PTW is an effective reinforcer and prepare PA/PTW composites by the method of dissolution-precipitation can avoid the

negative effect of PTW structure to SLS process. Nanoparticles such as clay and nano-silica can reinforce polyamide 12, but it has a negative to SLS as it absorb solvent, it is need research farther.

ACKNOWLEDGEMENTS

REFERENCES

[1] Seitz S, van de Crommert S, Esser KJ. SPIE 3102: 106-111.

[2]Holtzberg, Matthew W. Method for rapid production of structural prototype plastic parts. UP: 6,103,156.

[3]Dickens Jr., Elmer Douglas et.al. Sinterable semi-crystalline powder and near-fully dense article formed therein UP: 5,648,450.

[4] Kumar S. et.al. JOM, 2003, 55(3): 43-47.

[5]Kim J, Creasy TS. Polym. Test., 2004, 23: 629-636.

[6]Zarringhalam H, Hopkinson N, Kamperman NF. Materials Science and Engineering: A, 2006, 435-436(5): 172-180.

[7] Salmoria GV, Leite JL, Ahrens CH, et.al. Polym. Test., 2007, (1): 1-8.

[8] Caulfield B, McHugh PE, Lohfeld S. Journal of Materials Processing Technology, 2007, 182: 477–488.

[9] Wang Y. Study on the Polymer Materials of Selective Laser Sintering and the Properties of Sintered Parts. Ph.D Thesis, Huazhong university of Science and Technology, China, 2005.

[10]Yuan Q., Jiang W., An LJ, et al. Journal of Applied Polymer Science, 2003, 89(8): 2102-2107.

[11] Mazzoli A., Moriconi G., Pauri MG. Materials and Design, 2007, 28: 993－1000.

[12]Wang Y., Shi Y., Huang S. Processings of the Institution of Mechanical Engineers Part L, 2005, 219(L1): 11-15.

[13]Tjong SC, Meng YZ. Polymer, 1998, 39 (22) : 5461-5466.

[14]Qu MJ, Jian XG, HE W. Composites Materials Science & Technology, 2004, 12(4): 112.

[15] Childs THC, Tontowi AE. Journal of Engineering Manufacture, 2001, 215 (11): 1481.

[16] Chung H., Das S. Materials Science and Engineering A, 2006, 437: 226–234.

[17]Chen EF, CHEN D. polymer materials science and engineering, 2006, 22 (3): 1124-1135.

[18]Scholten, Heinz, Christoph. Wolfgang Use of a nylon-12 for selective laser sintering. UP: 6,245,281.

[19]Cui XL. China Fine Chemistry, 1996, 13 (4) 41-45.

[20]HE SQ, Li Y, Zhu CS. China Plastics Industry, 2004, 32 (2): 39-40.

[21]Zuo L, Mo X, Chen SM. J. Shenyang Polytechinc University, 1999, 1(4): 367-369.

[22]Sun MM. Physical modeling of the selective laser sintering process. Ph.D. Thesis, The University of Texas at Nustin 1991.
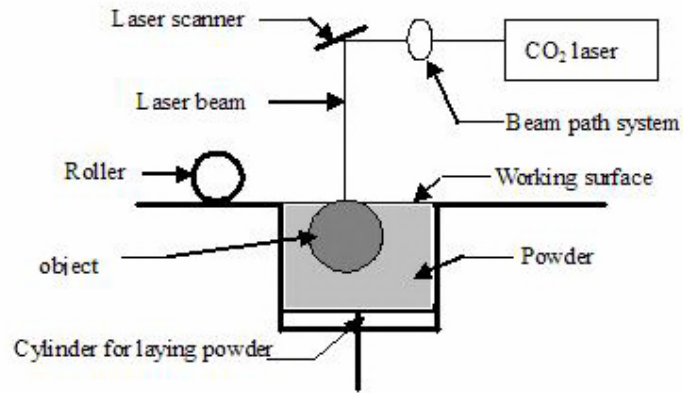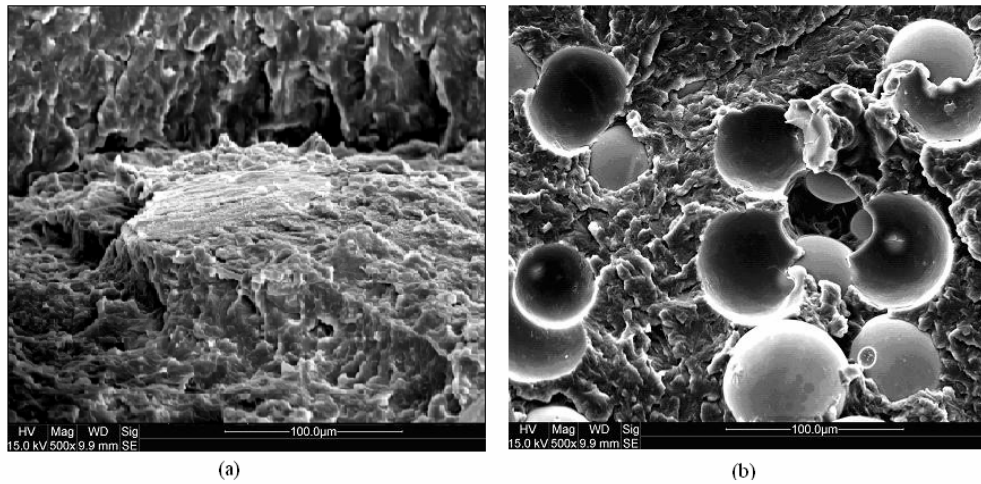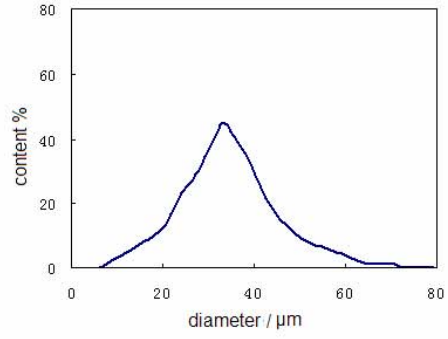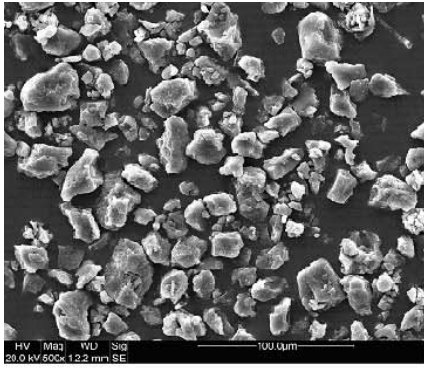
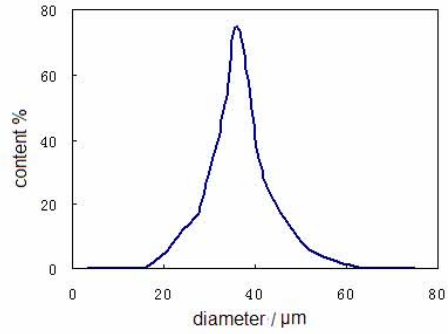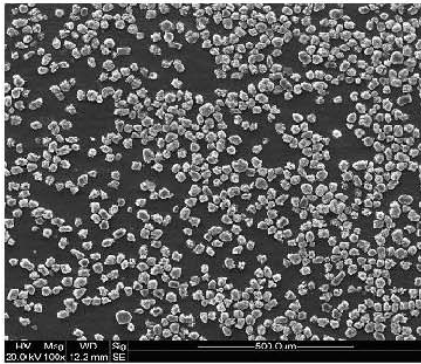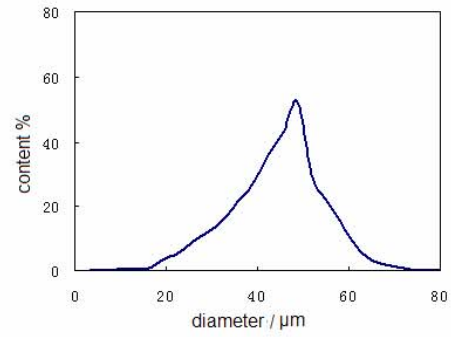Figure 1 Schematic illustration of the SLS process
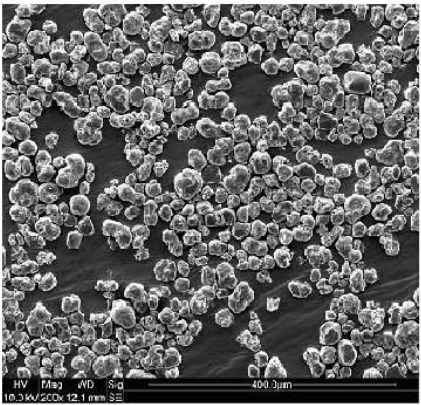

Figure 2   SEM images of PA12 and PA/GF sample impact fracture

(a) PA12 and (b) PA/GF (40 wt%)

(a)

(b)

(c)
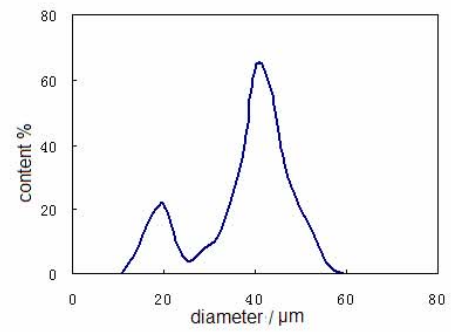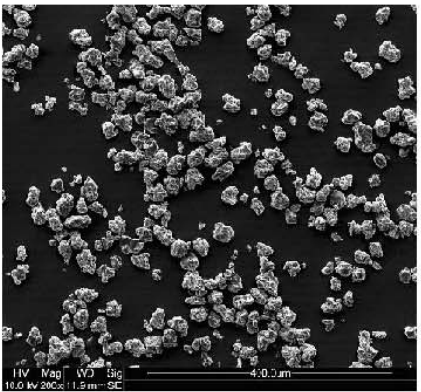
(d)

Figure 3   SEM images and particle diameter distribution curves of PA12 and PA/PTW powders
(a) PA12; (b) PA/PTW (10 wt%); (c) PA/PTW (20 wt%); and (d) PA/PTW (30 wt%)
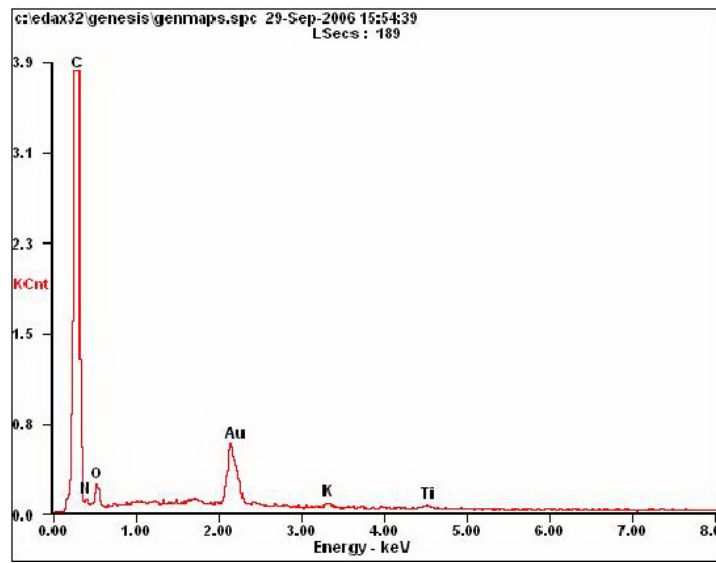
Figure 4 EDX of PA/PTW (20 wt%) powders

Figure 5 SLS specimen of PA/PTW (30 wt%)

(a)

(b)

(c)

(d)

Figure 6 SEM images of PA/PTW impact fracture

(a, b) PA/PTW (10 wt%) and (c, d) PA/PTW (30 wt%)

Figure 7 SEM images of PA/clay (3 wt%) powder obtained from dissolution-precipitation

(a)   (b)

Figure 8   SEM images of PAE(a) and PAE/NSi(0.5%) (b)
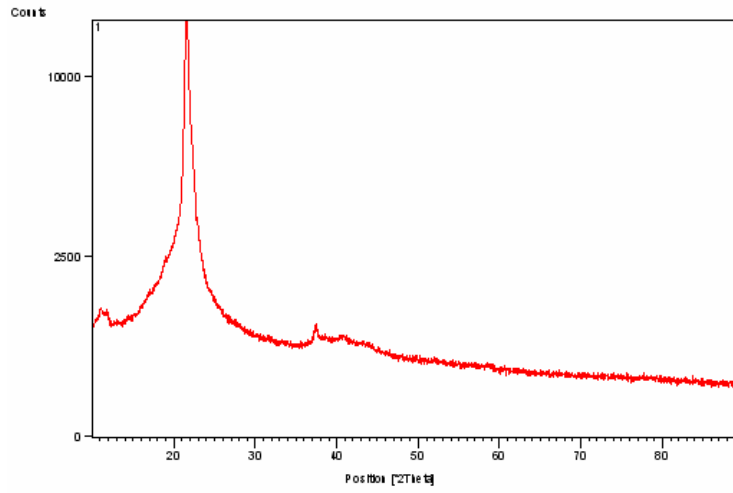
Figure 9 XRD of PA12 powder
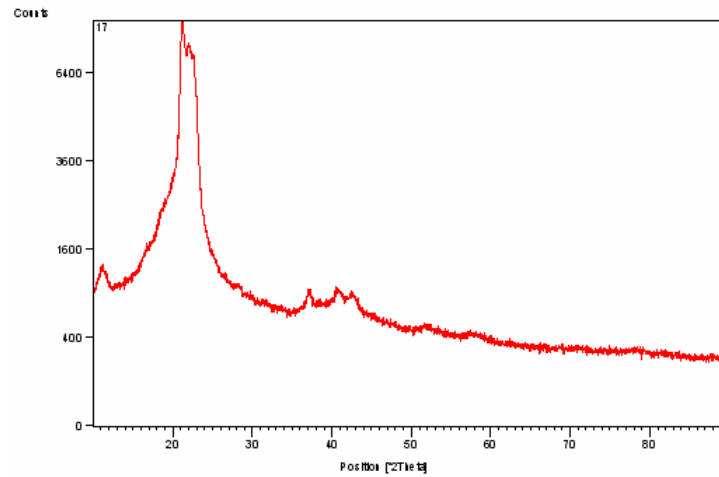
Figure 10 XRD of PAE alloy powder
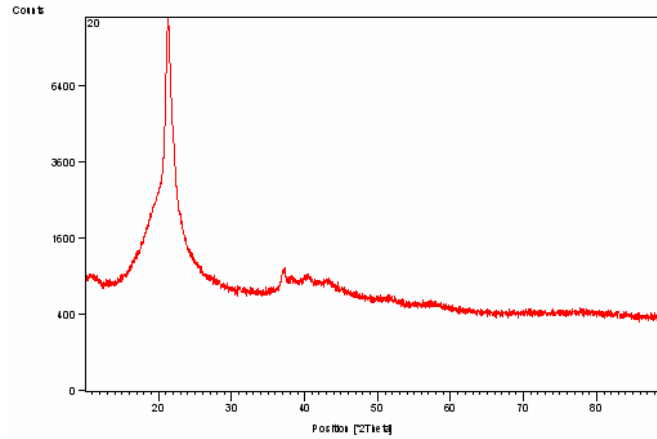
Figure 11 XRD of PAE/NSi powder

Table 1 mechanical properties of PA12 and PA/GF

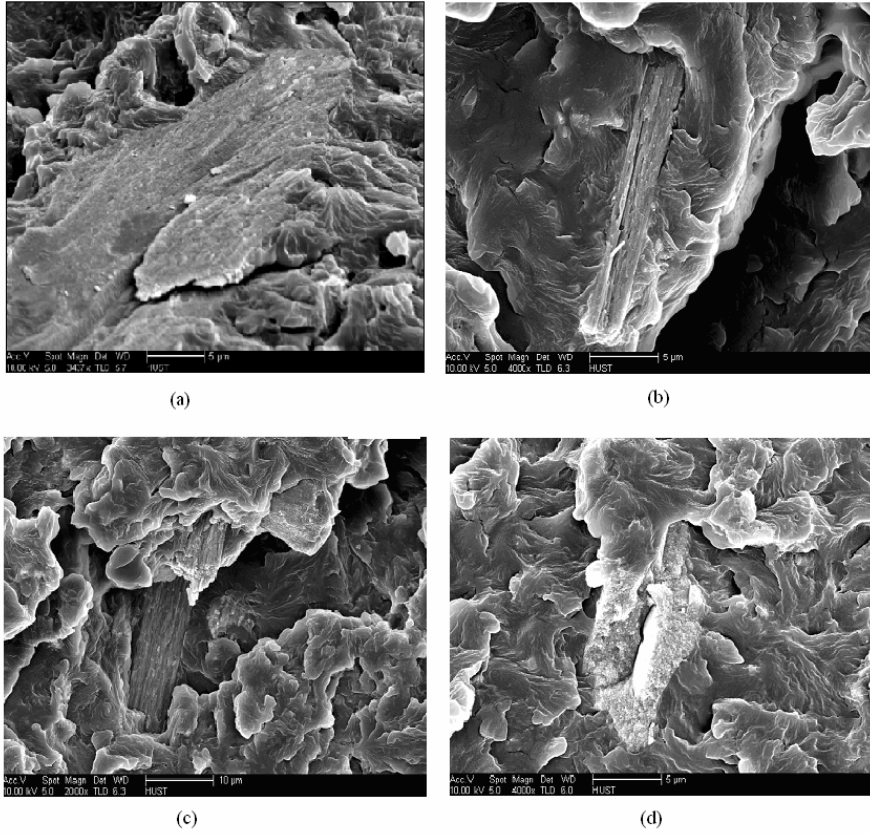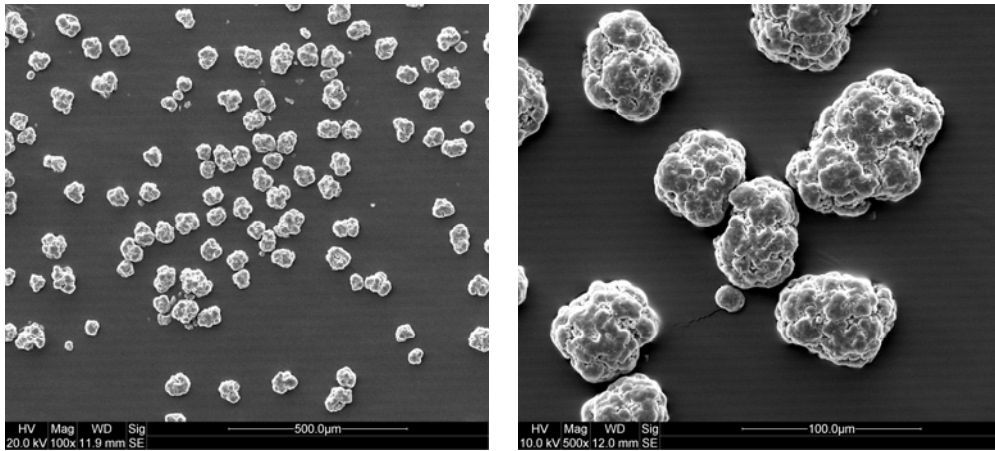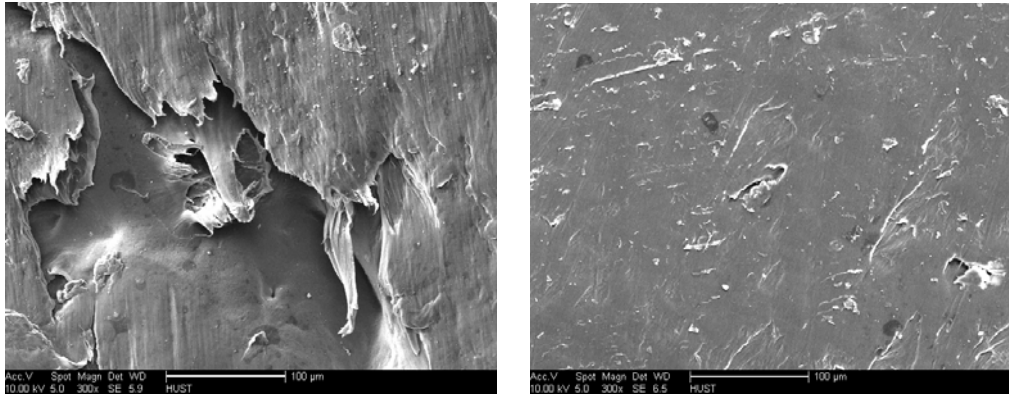|	PA12	PA/GF (30 wt%)	PA/GF (40 wt%)	PA/GF (50 wt%)
Tensile strength (MPa)	44.0	44.5	45±3.01	45.3±2.06
Impact strength(KJ/m^2)	37.2	20.9	18.7±1.38	15.3±1.03
Bending strength (MPa)	50.8	59.8	60.7±4.25	59.4±2.91
Bending modulus (MPa)	1.14	1.68	1.84±0.080	1.81±0.071

Table 2　Powder characteristics of PA12 and PA/PTW powders

	Diameter		Apparent density /(g/cm^3)
	Mean diameter/μm	Std. Deviation	
PA12	34.90	11.03	0.41
PA/PTW (10 wt%)	36.66	7.20	0.45
PA/PTW (20 wt%)	44.49	10.04	0.40
PA/PTW (30 wt%)	38.01	10.10	0.33

Table 3 Mechanical properties of PA/PTW samples

	PA/PTW (10 wt%)	PA/PTW (20 wt%)	PA/PTW (30 wt%)
Tensile strength (MPa)	52.5±2.78	68.3±6.31	52.7±9.36
Impact strength(KJ/m^2)	34.3±2.98	31.2±2.45	20.3±4.96
Blending strength (MPa)	72.2±5.20	110.9±6.54	85.3±3.93
Blending modulus (MPa)	1.52±0.14	2.83±0.39	2.68±0.16

Table 4 Mechanical properties of PA/clay samples

Materials	Sintering	Tensile strength	Flexural	Impact strength

	temperature(℃)	(MPa)	strength (MPa)	(KJ/m2)
PA/clay	169~170	48.7	64.3	31.2

Table 5 sintering characteristics and mechanical properties of PAE and PAE/NSi

	PA12	PAE	PAE/NSi (0.5%)
Sintering temperature(℃)	167~169	123~160	128~160
Density(g/cm^3)	0.96	0.93	0.93
Tensile strength (MPa)	44.0	29.8	38.7
Impact strength(KJ/m^2)	37.2	48.6	45.2
flexural strength (MPa)	50.8	34.9	45.0
flexural modulus (MPa)	1.14	0.87	1.05

Electrical and dielectrical properties of the epoxy-hematite nanocomposites

V. Djoković*#, D. Dudić, N. Jović, M. Marinović-Cincović, J. M. Nedeljković

Vinča Institute of Nuclear Sciences, P. O. Box 522, 11001 Belgrade, Serbia,

Email id: djokovic@vin.bg.ac.yu

Abstract

α-Hematite nanorods were used as filler for the epoxy resin. Electrical and dielectrical properties of the obtained nanocomposite were investigated. DC-conductivity measurements showed a significant influence of Fe_2O_3-nanorods on the DC-electrical properties of the epoxy matrix. However, the observed effects of the filler below and above the glass transition are different. Because of their high specific surfaces, nanorods affected segmental mobility of epoxy molecules to a large extent, which resulted in an increase in the glass transition temperature (T_g) and a decrease in the real part of dielectric permittivity in high frequency/low temperature region.

Introduction

Nanostructured semiconductor-polymer hybrids have been intensively studied in the last two decades because they provide opportunities for preparation of novel high-performance materials that exploit the synergism of the characteristic physical properties of both components [1-2]. However, only recently attention has been paid to possible use of nano-dilectric fillers in order to improve dielectric properties of the polymer matrix [3-7]. The former studies suggested that introduction nano-dielectric fillers in polymers can be beneficiary in terms of improved discharge resistance, dielectric strength and thermal conductivity. For example, contrary to the micron sized TiO_2 [3] and $BaTiO_3$ [5] fillers, which increase the real part of the dielectric permittivity (ε') of the epoxy matrix, nano-dielectric fillers of the same type showed an opposite effect. Taking into account the above mentioned trends, in the present study, we investigate the electrical properties of the composites of epoxy and α-Fe_2O_3 nanorods.

Experimental

Preparation of hematite (α-Fe₂O₃) nanorods
Dispersions of α-Fe2O3 nanorods were prepared by "forced hydrolysis", i.e., thermal hydrolysis of iron(III) chloride solution. 100 ml 5.4 M NaOH was added to 100 ml 2 M $FeCl_3$ and the solution was stirred at room temperature for 15 min. After that, the solution was heated up to 100 °C and kept at that temperature for 8 days. The α-Fe_2O_3 nanorods were recovered by centrifugation at 3000 RPM for 15 min, washed out several times with water and dried in vacuum. TEM measurements (not shown) revealed that the obtained nanorods have the average diameter of 8 nm and average aspect ratio of 25.

Preparation of epoxy-hematite nanocomposites
In order to prepare the nanocomposites, a desired amount of previously synthesized hematite nanorods was immersed into diglycidyl ether of Bisphenol-A (DGEBA) prepolymer. The mixture is sonicated for 3 hours in order to get a uniform dispersion of the nanorods within the resin. After

that, the curing agent aminomethyl 3, 3, 5- trimethylcyclohexylamin was added with continuous stirring (the epoxy-curing agent ratio was 3:1 by weight). Finally, the mixture was cast into a flat glass mold and outgassed overnight. Before they were taken out from the mold, all samples were postcured at 110 °C for 10 minutes in air. The obtained planar composite samples had an approximate thickness of 1 mm. Because of the high aspect ratio of the nanorods, the content of the inorganic phase in the composite was chosen to be 2 wt.%.

Apparatus
Electrical DC conductivity measurements were performed in a shielded cell using Agilent 4339B high resistance meter. Samples were in the form of thin disks 0.9-1 mm thick and about 13 mm in diameter. Electrodes were made on the major faces using silver contact paste. The temperature dependences of the specific conductivity of the pure epoxy and the epoxy-hematite nanocomposite films were measured in the range from 20 to 127 °C. The heating and cooling rates were 2 °C/min and a constant current of 2 nA was set during the measurements. Dielectric spectroscopy measurements were performed on an Agilent 4284A instrument in the frequency range between 20 and 10^6 Hz and temperature range from 25 to 152 °C. The preparation, the shape and the conditioning of the samples were the same.

Results and Discussion

The specific conductivity changes of the pure epoxy and the epoxy-hematite nanocomposite during the heating-cooling cycle are shown in Fig. 1. Although both materials exhibit conductivity hysteresis, a slightly different behaviour below and above the glass transition temperature (~50-60 °C) can be noticed (the influence of the nanorods on the glass transition temperature of the matrix will be discussed further in the text). Up to the glass transition temperature, the magnitude of changes of the specific conductivity of the pure epoxy is much higher than that of the nanocomposite, while an opposite effect can be observed after the materials begin to soften (Fig. 1). Eventually, in the investigated temperature range, overall conductivity changes of about five orders of magnitude are noticed for both materials. A slower increase in the DC conductivity of the nanocomposite could be explained by the lower mobility of the epoxy segments in the presence of high specific surface fillers. Nevertheless, the change in the curing conditions, probably due to an increased proportion of hardener in the vicinity of nanorod surfaces [3], could also contribute to the observed DC conductivity behaviour of the nanocomposite. The glass transition temperature of the pure epoxy and the epoxy-α-Fe$_2$O$_3$ nanocomposite was determined using a modified empirical Vogel-Tammann-Fulcher-Hesse (VTFH) equation [8]:

$$\sigma_{dc} = \sigma_{dc0} \exp\left[-\frac{DT_0}{T-T_0}\right], \tag{1}$$

where σ_{dc0}, D and T_0 are fitting parameters. The VTFH equation describes well the dependence of the specific conductivity as well as the dipole relaxation times on the reciprocal temperature in the regions close to the glass transition. Therefore, by fitting experimental results in Fig. 1 to Eq. (1) it is possible to obtain parameters T_0 (the so-called Vogel temperature) and D (strength parameter) which are related to the glass transition temperature, T_g, by the following empirical expression [9,10]:

$$T_g = T_0(1+0.0255D). \tag{2}$$

Fig.2 shows the dependences of specific conductivity on the reciprocal temperature for data presented in Fig.1 while the fits to Eq. (1) are given by the solid lines. The obtained fitting parameters and the corresponding glass transition temperatures estimated through Eq. (2) of two

samples are shown in Table 1. The results in Table 1 show that the glass transition of the epoxy matrix in the presence of α-Fe$_2$O$_3$ nanorods is shifted by 9 degrees towards higher temperature compared to pure epoxy (from 47 to 56 °C). This means that α-Fe$_2$O$_3$ nanoparticles indeed reduce the mobility of the matrix bellow the softening point and consequently slow down the conductivity increase with increasing temperature observed in Fig. 1.

Fig. 3(a) shows the real part of dielectric permittivity ($\varepsilon' = \varphi(f, T)$) of the pure epoxy as a function of frequency and temperature. It can be seen that at low frequencies ε' increases with increasing temperature. An apparent step in ε' values can be noticed at 10^2-10^3 Hz and at temperatures above 80 ° C. In this frequency/temperature region dielectric properties are largely controlled by charge transfer processes (the conductivity relaxation and the space charge polarization) [6,7,11]. The dielectric loss results ($\varepsilon'' = \varphi(f, T)$) of the pure epoxy in Fig. 3(b) support the former conclusion. In the low frequency-high temperature regions there is a linear dependence of log ε'' from log f with a slope close to -1 (linear regression in the range from 10^1-10^3 Hz gives a value of -0.98). In order to illustrate it more clearly, we included log $\varepsilon''= \varphi(\log f)$ curves taken at 120, 140 and 152 °C as the inset of Fig. 3(b). The value -0.98 obtained in the linear regression of log $\varepsilon''= \varphi(\log f)$ curves is typical for the presence of conductivity current relaxation [12]. Real ($\varepsilon' = \varphi(f, T)$) and imaginary ($\varepsilon'' = \varphi(f, T)$) parts of the complex dielectric permittivity of the epoxy-α-Fe$_2$O$_3$ nanocomposite show similar functional dependence on frequency/temperature to that of the pure epoxy matrix (Fig. 3) and they will not be presented here. On the other hand it is worth to mention that there is a change in the magnitude of the real part of the dielectric permittivity of the epoxy-hematite nanocomposite (ε'_{EH}) with respect to that of the pure epoxy resin (ε'_{ER}). We illustrate this in Fig. 4, where the relative change of dielectric permittivity (defined as $\Delta\varepsilon' = 100\times(\varepsilon'_{EH}-\varepsilon'_{ER})/\varepsilon'_{ER}$) is plotted vs. frequency and temperature. It can be seen that $\Delta\varepsilon'$ is about -10%, except in the range of temperatures of 100-152 °C and low frequencies. This means that in the low temperature/high frequency regions ε' of the nanocomposite decreases due to reduced segmental mobility of the matrix, induced by α-Fe$_2$O$_3$ nanorods. The nanorods immobilize to a certain extent the end-chain and/or the side-chain movement of the epoxy molecules, which influences the molecular polarization and consequently reduces the permittivity of the matrix. Similar effects of the nanofiller on the dielectric permittivity of the epoxy resin have been noticed by several authors/groups [3,5,6,7].

References

1 Balazs AC, Emrick T, Russell TP. Science 2006;314:1107-1110.
2 Godovsky DY. Advan Polym Sci 2000;153:163-205.
3 Nelson JK, Fothergill JC. Nanotechnology 2004;15**:**586–595.
4 Nelson JK, Hu Y. J Phys D Appl Phys 2005;38:213–222.
5 Tuncer E, Sauers I, James DR, Ellis AR, Paranthaman MP, Aytug T, Sathyamurthy S, More KL, Li J, Goyal A. Nanotechnology 2007;18:025703 (6pp).
6 Kanapitsas A, Pissis P, Kotsilkova R J. Non-Cryst Solids 2002;305:204–211.
7 Pissis P, Fragiadakis D. J Macromol Sci B Phys 2007;46:119-136.
8 Angell CA. J Non-Cryst Solids 1991;13:131-133.
9 Polizos G, Shilov VV, Pissis P. Solid State Ionics 2001;145:93-100
10 Angell CA. Annu Rev Phys Chem 1992;43:693-717.
11 Nikonorova NA, Barmatov EB, Pebalk DA, Barmatova MV, Domínguez-Espinosa G, Diaz-Calleja R, Pissis P. J Phys Chem C 2007;111:8451-8458.
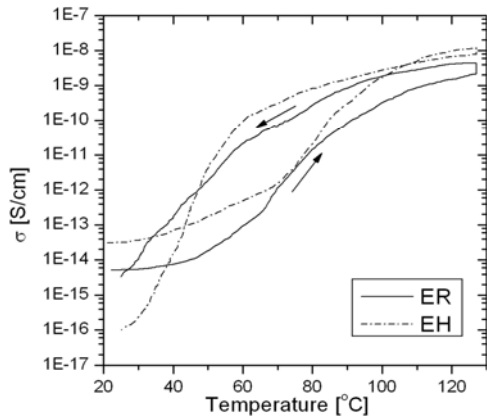12 Hedvig P. Dielectric spectroscopy of polymers, Akadémiai Kiadó, Budapest, 1977.

Fig. 1. The DC-conductivity dependence of the pure epoxy (ER) and the epoxy-hematite (EH) nanorod composite on temperature
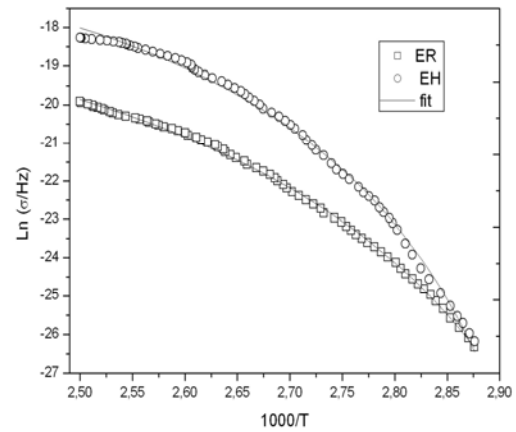

Fig. 2. Dependence of ln σ_{DC} on the reciprocal temperature for the epoxy and epoxy- hematite nanocomposite. The fit to the Eq. (1) is given by solid line.
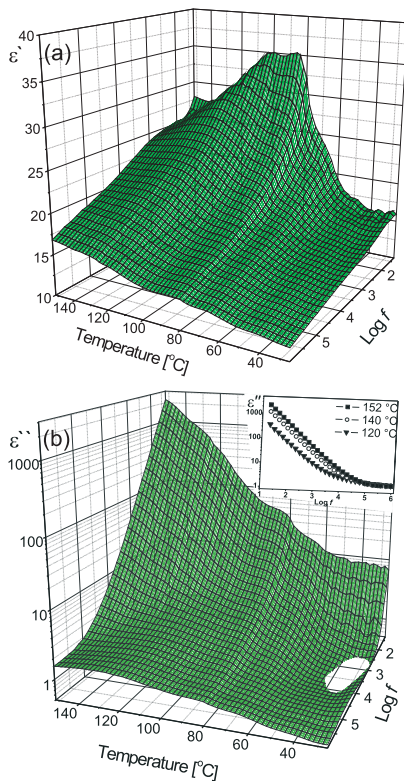
Fig. 3. (a) The real and (b) imaginary parts of dielectric permittivity of the pure epoxy resin as a function of temperature and frequency. Inset: ε'' vs. frequency at 120, 140 and 152 °C.

Table 1. Parameters of the Eq. (1) obtained from the curves in Fig. 2. The glass transition temperatures (T_g) were obtained using Eq. (2).

sample	σ_{dc0}, S/cm	T_o, K	D	T_g, °C
ER	$8,4\ 10^{-5}$	308,9	1,41	47,0
EH	$2,9\ 10^{-5}$	320,7	1,07	56,4

Fig. 4. Relative changes of $\Delta\varepsilon'$ of the real part of dielectric permittivity (defined as $\Delta\varepsilon'=100\times(\varepsilon'_{EH}-\varepsilon'_{ER})/\varepsilon'_{ER}$) after the introduction of α-Fe_2O_3 nanorods into epoxy resin (ER).

A reactive nanoparticle route to prepare hybrid nanocomposites

Patricia Heiden
Michigan Tehcnological University, Houghton, Michigan, USA
Emal: paheiden@gmail.com

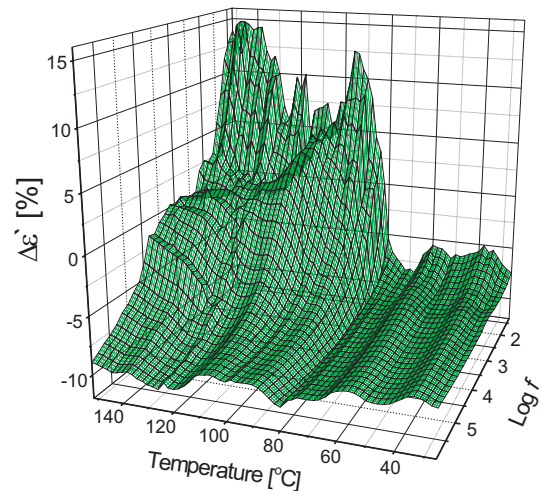Hybrid nanocomposites having nanoscale inorganic domains dispersed within an organic polymer can afford materials with a synergistic combination of properties that are characteristic of the inorganic and organic components of which they are comprised. The ability to obtain materials with select properties from the organic and inorganic components allows these materials to find uses in optical, electrical, biomedical, and other specialty areas. The inorganic phase can be pre-made and blended into a polymer melt or solution, which allows precise control of composition, but blending is energy-intensive, and often the dispersed phase does not interact effectively with the matrix, so properties might not be optimized, and the dispersed phase may not be stable. Alternatively, a reactive pre-cursor to the inorganic species may be blended into the polymer melt or solution and reacted to produce the inorganic phase in situ in a sol-gel reactive. This often allows better dispersal of the inorganic phase and better interaction between the two phases, but offers less control over composition, and many reactive precursors are so highly reactive that they phase separate into macroscale, rather than nanoscale domains, and so choice of both reactive precursor and organic matrix is often limited. Here we describe a reactive nanoparticle route that allows hybrid nanocomposites to be prepared with comparatively few limitations on composition by incorporating the reactive precursor into a nanoparticle and converting it to the inorganic component in situ before the final film formation. Effects of synthetic variables are described on the reaction process and film properties.

Key words: nanocomposites, inorganic phase, reactive precursor

Polymer nanocomposites for functional applications

Franz Faupel[1#], Vladimir Zaporojtchenko[1], Henry Greve[2], Ulrich Schürmann[2], Haile Takele[1], Christian Hanisch[1], Venkata Sai Kiran Chakravadhanula[1]*, Amit Kulkarni[1], A. Gerber[2], Eckhard Quandt[2], and Rainer Podschun[3]

[1]Christian-Albrechts-Universität zu Kiel, Institut für Materialwissenschaft, Lehrstuhl für Materialverbunde, Kaiserstr. 2, D-24143 Kiel, Germany.
[2]Christian-Albrechts-Universität zu Kiel, Institut für Materialwissenschaft, Lehrstuhl für Anorganische Funktionsmaterialien, Kaiserstr. 2, D-24143 Kiel, Germany.
[3]Christian-Albrechts-Universität zu Kiel, Institut für Infektionsmedizin, Universitätsklinikum Schleswig-Holstein, Campus Kiel, Brunswiker Str. 4, 24105 Kiel, Germany
Email: [#] ff@tf.uni-kiel.de, * cv@tf.uni-kiel.de

While extensive research has been carried out in the field of structural polymer-based nanocomposites, much less investigations have been concerned with polymer nanocomposites for functional applications. Among the functional nanomaterials, nanocomposites consisting of metal nanoparticles dispersed in a dielectric matrix are of particular interest due to their novel functional properties offering hosts of new applications. Here, polymers are attractive as matrix, and several approaches have been reported to incorporate metal nanoparticles into polymers.

The present talk is concerned with the preparation of polymer-based nanocomposites by vapor phase co- and tandem deposition and the resulting functional properties. The techniques involve evaporation and sputtering, respectively, of metallic and organic components and inter alia allow the preparation of composites which contain alloy clusters of well defined composition. Emphasis will be placed on soft-magnetic high frequency materials with cut-off frequencies well above 1 GHz and high quality factors and on optical composites with tuned plasmon resonances suitable for ultra thin color filters, Bragg reflectors, and other devices. In addition, antibacterial coatings and selective sensors for organic vapors based on nanocomposites with filling factors close to the percolation threshold will be addressed. Moreover, a novel approach to produce magnetic nanorods for potential applications in high-density data storage and other fields will be presented.

Keywords: polymers, nanocomposites, coatings, nanoparticles, nanorods, evaporation, sputtering, magnetic, high frequency, antibacterial, optical

Mechanical behavior, processing and characterization of biocomposites

Song-Jeng Huang*, Hsing-Ching Tsao**

Department of Mechanical Engineering, National Chung Cheng University

168, University Rd., Ming-Hsiung, Chia-Yi, 621, Taiwan, ROC

Email: * ime_hsj@ccu.edu.tw , ** tsao1319@yahoo.com.tw

Natural fibers are increasingly used as reinforcement in commercial thermoplastics due to their low cost, high specific properties and their renewable nature, as well as the environmental concerns and a shortage of petroleum resources. In this study, the mechanical behavior of biocomposites based on biodegradable polymer matrix (PLA) was investigated. Two different kind of natural fibers using pineapple leaf and rice stem fiber as reinforcements were prepared, respectively. The natural fiber and PLA pellet were mixed and biocomposites were fabricated using a compression molding method. Regarding the chemical treatment, maleic anhydride (MA) was used as a compatibilizer between fiber and matrix. Alkali treatment can remove the lignin, oil and other impurity on the surface of the fiber. The mechanical behavior of present biocomposite is estimated to be better than that of pure PLA.

Key words: biocomposites, natural fiber, mechanical behavior, processing

Preparation and properties of thermoplastic polyurethane nanocomposites by melt blending: effect of organoclay on mechanical, thermal, morphological and dynamic mechanical properties

A. K. Barick & D. K. Tripathy*
Rubber Technology Centre, Indian Institute of Technology
Kharagpur, West Bengal, INDIA, PIN – 721302
Email: dkt@rtc.iitkgp.ernet.in

Polymer nanocomposites based on medical grade thermoplastic polyurethane (TPU) and organically modified montmorillonite (OMMT) has been prepared by melt intercalation technique using a Haake batch mixer at 185°C with a rotor speed of 100 rpm and mixing time of 6 minutes. Varying amount of organically modified nanoclays (1, 3, 5, 7, & 9 wt %) was added to the TPU matrix in order to examine the influence of the organoclay on nanophase morphology and materials properties. The interactions between TPU matrix and nano filler were evidenced by FTIR spectra of the TPU/OMMT nanocomposites. XRD, TEM & SEM analysis showed that melt mixing by a batch mixer was effective in dispersing OMMT through the TPU matrix. The X-ray analysis revealed that exfoliation occurred for low montmorillonite content, whereas for higher contents the intercalated clays get rearranged to a minor extent. It is evident from the TEM images that the nanoclay stacks were smaller and more evenly distributed in the composites prepared by melt intercalation. The aggregated clay morphology was characterized with SEM. Because of the difference in scattering density between the clay and PU, large clay aggregates can be easily imaged in SEM. Nanoparticle dispersion was the best at 5-wt % of OMMT. Nanocomposites exhibit higher mechanical, dynamic mechanical and thermal properties than that of pristine TPU matrix, which increases with the increase in OMMT content. The mechanical properties showed an improvement of the elastic modulus, tensile strength and elongation at break but a decrease in the stress and strain values at breaking point on increasing the clay content. TGA data revealed that 5-wt % incorporation of organoclay enhances the thermal stability of nanocomposites significantly. Melting point and glass transition temperature of soft segments were found to shift towards higher temperature with the inclusion of organoclays. DSC data revealed Tg, crystallization and melting temperature of polyurethane matrix are shifting towards the higher temperature with inclusion of nanoclays. Rheological behavior of TPU nanocomposites were characterized by rubber process analyzer. DMA result indicates that below the T_g, addition of OMMT has strongly influenced the elastic (corresponding to E') and plastic (corresponding to E'') properties of the TPU matrix. Significant enhancement of E' and E'' can be seen for the TPU/OMMT. This is due to the mechanical reinforcement resulting from strong interaction between OMMT and the TPU matrix for the enhancement of E', and the improvement of E'' indicates that plastic response to the deformation is prominent in the presence of the OMMT.

Key words: medical grade TPU, organoclay melt processing, DMA, TGA, RPA

Polymers for space applications

Dr. K N Ninan

Vikram Sarabhai Space Centre, Thiruvananthapuram - 695022

Email: kn_ninan@vssc.gov.in

A number of exotic materials having a wide range of properties are required for accomplishing various space missions. These requirements are met to a large extend by the use of high performance polymers. The most important polymeric system used in satellite launch vehicle is the polymeric fuel binder for composite solid propellants. The present day binders have a polybutadiene backbone. Hydroxyl terminated polybutadiene (HTPB) is the sate of the art binder which has been developed and produced in-house. Polymer based insulations and inhibitors are used to protect the rocket motor case and to give the desired burning pattern to the propellant grain.

Thermal protection systems are another class of polymeric systems used in rockets and satellites and silicone resins are widely used as coatings in this regard. Preceramic polymers, which give ceramic residue on pyrolysis at 1500°C, find applications as oxidation resistant coatings. Phenolic resins continue as the material of choice for making ablative liners of rocket nozzles and re-entry vehicles that encounter very high heat flux. The high thermal stability of polyimides makes them ideal candidates as thermal control barrier in satellites.

Polymer matrix composites have many applications in aerospace industry. Epoxides, cyanate esters, bismaleimides, polyether ketones etc are the matrices of choice, while polyaramid fiber and polyacrylonitrile co-polymer based carbon fibers are the most widely used reinforcements. Since aerospace structures consist of dissimilar materials, different adhesives are used for joining them. The use of cryogenic fluids as propellants poses the challenge for developing compatible thermal insulations.

Reusability of the launch vehicles is a major step towards the reduction of launch cost. This calls for the development of polymers capable of withstanding higher heat fluxes and oxidizing environments, for which carbon-carbon and ceramic matrix composites are developed. Interplanetary missions of the future need materials of high specific strength which are able to withstand hard vacuum and hostile environment of very low and high temperature, cosmic radiation etc. Intelligent materials are needed for long duration and far off missions. Such challenging future demands of the space industry give enormous opportunities for developing new high performance polymers and tailoring the existing ones for specific missions.

Key words: high performance polymers, polymeric fuel binder, preceramic polymers, thermal insulations

Composition effects on proton conductivity of hybrid polysiloxane membranes

Martin Mika[*#] **, Jakub Michal, Bretislav Klapste, Petr Hron**

Institute of Chemical Technology, Technicka 5, Prague, Czech Republic 166 28
Email: Martin.Mika@vscht.cz

Burning carbon based fuels has been for centuries the most common technology how to produce energy. Nowadays, the growing demand for energy has caused the steep increasing of CO_2 concentration in the atmosphere for last several years. This development could cause serious climate changes and the flooding of areas close to seashore. The solution how to reverse this trend is switching from carbon fuels to carbon-free, namely hydrogen. To economically produce electric energy from hydrogen we need effective H_2/O_2 fuel cells equipped with high proton conducting membranes. In our laboratory we have developed fast proton conducting hybrid membranes that can be applied in the H_2/O_2 fuel cells operating in dry conditions at room and elevated temperatures. The main constituent of the membrane is the polydimethylsiloxane polymer with phosphorous heteroatoms. As the most important property of the membrane is its high proton conductivity, we developed the synthesis procedure that guarantee the high concentration of stable hydroxyl groups promoting the fast proton migration. To enhance the conductivity, we fill the polymer with SiO_2 nanoparticles and achieve the conductivities about 0.02 S/cm at 130°C in dry atmosphere. The conductivity is precisely determined by using impedance spectroscopy. The membrane is placed into the electrochemical cell with Pt electrodes and its impedance is measured in the frequency range from 0.01 Hz to 1 MHz at temperatures from 25 to 180°C. The recorded impedance data are analyzed in the Nyquist complex plane diagram using the equivalent circuit approach. In our paper we discuss the effects of membrane's components and the influence of the preparation procedure on the membrane's proton conductivity and its performance in the laboratory H_2/O_2 fuel cell.

Key words: fuel cells, proton conductivity, polydimethylsiloxane, SiO_2 nanoparticles, impedance spectroscopy

Rubber in underwater sensor technology

Dr.V B Pillai
Naval Physical and Oceanographic Laboratory, Kochi 682021
Email: vbpillai@gmail.com

Rubber is extensively used in the underwater acoustic sensor scenerio. The applications include transducer encapsulants, sound absorbers, acoustic window materials, acoustic baffles, shock and vibration isolators, seals, 'O' rings etc. Underwater transducers operate over large ranges of frequency, temperature and pressure. The marine environment in which the transducers are deployed represents one of the most variable and a harsh environment with its corrosive saline water, salt laden above–water atmosphere, wind, waves, tides etc. The service life normally expected for underwater transducer is 15-20 years. It is important that rubber used for the protection of sensors, in addition to being able to sustain the mechanical rigours of the marine environment, must be able to withstand severe stresses imposed by temperature extremes, ozone attack, and the chemical attack of seawater, pollutants, and physical abuse. A number of physical, chemical, electrical, mechanical and acoustic characteristics have been identified as critical for efficient and reliable system behaviour. The technology involved in tailoring the basic rubber material so as to perform different functions such as sound absorbers, reflectors, window materials, acoustic baffles etc., has been evolved and matured. The talk will address the major issues involved in the development of rubbers for underwater sensors applications.

Conventional engineering of rubbers does not suffice to meet with the exact, often stringent performance specifications envisaged for passive acoustic rubbers. The material should satisfy a set of complex and demanding end-use situations imposed by the marine environment, material limitations, and application specific requirements. The major parameters include (1) water absorption & permeation (2) electrical resistivity (3) dynamic mechanical properties (4) acoustic impedance (5) bondability to metal (6) ease of processing (7) permanence of properties etc. Performance of the rubber in terms of both short and long-term properties is understood as a function of composition, cures condition and environmental parameters. Each parameter is to be optimized through judicious compound development and characterization. An optimised formulation is thus designed and its quality –control techniques developed to guarantee the reproducibility of intended performance.

The rubber vulcanisate during their service absorb substantial amount of water. The absorbed water may significantly alter the performance characteristics leading often to product

failures or de-rated performance. Problem has been successfully addressed in the case of neoprene rubber with the development of a patented curing process.

Underwater transducers are basically high voltage electrical devices and hence their electrical insulation should be high and stable. Use of carbon black is imperative for optimum mechanical properties, whereas inclusion of carbon black in large quantities is detrimental for electrical insulation, particularly for Neoprene. The amount and type carbon black for optimal behaviour has been developed. Transducers are also dynamic devices operating in a wide frequency band and temperature range. Rubbers are visco-elastic materials characterized by wide variation of stiffness and damping with of frequency and temperature. Dynamic mechanical properties determine the acoustic behaviour of elastomers; thus, it is imperative that rubbers used for encapsulation be optimised for specific dynamic mechanical behaviour within the operating frequency band.

In the construction of a transducer, encapsulation material comes in the acoustic path between transducer and seawater. The intervening medium should not adversely affect acoustic wave propagation across it to the water medium. The product of density and sound velocity, the acoustic impedance, in the material decides the propagation losses. For reflection free transmission the acoustic impedance of mediums should match. This has been achieved by tailoring dynamic complex modulus and density of the rubber. Also, dynamic loss factor, tan delta, has been optimised to minimize sound attenuation. Material developed in NPOL serves as a perfect acoustic window with near zero echo reduction. The rubber compositions have been optimized for compound viscosity; scorch safety, cure characteristics, bonding to metals, and permanence of properties and ease of fabrication.

Conventional heat aging method of estimation of safe service life of rubber products has been substantiated by mathematical equation correlating elongation at break properties with Arrhenius model and curve fitting methods. However, they seldom reflect the effect of aging on functional properties of the transducers.

Estimation of service life of underwater elastomers is important from the point of fleet readiness and reliability. The controlling parameters selected are, water diffusivity and permeability, electrical resistivity, dynamic and static mechanical properties. Estimation of diffusion coefficient at accelerated environment allows prediction of the depth of penetration and hence the life. Permeation of water across the encapsulation rubber is another aspect that has been studied. The rate of permeation follows Arrhenius type temperature dependence. Continued permeation of water vapour through the barrier material can lead to high build up of moisture into the transducer, which can be modelled for reliable life prediction.

Some of the important parameters as out lined above will be discussed in the talk.

Conjugated polymer thin films for biosensing applications

Shilpa N. Sawant

Chemistry Division, Bhabha Atomic Research Centre, Mumbai 400 085

email: stawde@barc.gov.in

Conducting polymers are paving the way for 'all-organic' electronic devices and chips [1]. Though these materials have a large potential for application, they have not been utilized to full extent due to practical difficulties. Many of these material lack important properties required for practical application such as high conductivity, stability, processability etc. The ultimate usefulness of these fascinating materials hinges on a detailed understanding of their fundamental redox operation and the accompanying physico-chemical, structural changes. This talk focuses on our attempt for improving the physical properties of conjugated polymers and their application for biosensing. For *e.g.* Judicious selection of the dopant anion can help in improving the environmental stability of polyaniline [2]. By preparing an organic-inorganic hybrid it is possible to add extra functionality (*e.g.* magnetism) to polyaniline [3]. Polymerisation of a monomer in its Langmuir-Blodgett (LB) film results in an ordered film of the polymer with higher conductivity [4]. The processability of polyaniline can be improved by preparing its colloidal nanoparticles [5]. From the point of view of biosensing application, use of polyaniline for sensing analytes such as glucose and lindane will be discussed.

Another class of polymeric material of our research interest is polydiacetylenes (PDA) since its derivatives exhibit biochromatic properties. PDA can form self assembled Langmuir-Blodgett films which exhibit color changes from blue to red upon external stimuli like pH, mechanical stress etc [6]. Diacetylenes can be modified to incorporate various bio-specific receptors (e.g. enzymes, antibodies etc) and photopolymerised insitu. The resulting film can be used for detection of the corresponding substrate / ligand. For example, sialic-acid-derivatized polydiacetylenes detect influenza virus emagglutinin by a color change from blue to red [7]. In the present talk several examples of PDA based biosensor will be discussed along with our work on enolase [8] and glucose oxidase immobilized PDA LB films.

References:
1. Skotheim TR, Reynolds JR. editors, Handbook of Conducting Polymers, 3rd Ed, CRC Press, 2006.
2. Shilpa Tawde, Mukesh D, Yakhmi JV. Synthetic Metals 2002;125: 401.
3. Sawant SN, Bagkar N, Subramanian H, Yakhmi JV. Phil. Mag. 2004; 84(20): 2127.
4. Sawant SN, Mukesh D, Yakhmi JV, Kulshreshtha SK, Miyazaki A, Enoki T. J. Phys. Chem. B 2006; 110 (48): 24530 -24540
4. Hassan PA, Sawant SN, Bagkar NC, Yakhmi JV. Langmuir 2004; 20: 4874.
5. Charych DH, Nagy JO, Spevak W, Bednarski MD. Science 1993; 261: 585-588
6. Reichert A, Nagy JO, Spevak W, Charych DH. J. Am. Chem. Soc. 1995; 117: 829-830
7. Sadagopan K, Sawant SN, Kulshreshtha SK, Jarori GK. Sensors and Actuators B 2006; 115: 526–533.

Contact Nos:
022-25590288 (O)
09967664895